Proyecto Fin de Máster
Máster en Diseño Avanzado en Ingeniería Mecánica

Coupling of hydrogen assisted embrittlement with a modeling framework for the interaction between the phase field approach for brittle fracture and the interface cohesive zone model

Autor: Ángel de Jesús Valverde González

Tutor y publicador: José Antonio Reinoso Cuevas

Tutor externo: Adrià Quintanas Corominas

Dpto. Mecánica de Medios Continuos y Teoría de Estructuras
Escuela Técnica Superior de Ingeniería
Universidad de Sevilla

Sevilla, 2019

Proyecto Fin de Máster
Máster en Diseño Avanzado en Ingeniería Mecánica

Coupling of hydrogen assisted embrittlement with a modeling framework for the interaction between the phase field approach for brittle fracture and the interface cohesive zone model

Autor:
Ángel de Jesús Valverde González

Tutor y publicador:
José Antonio Reinoso Cuevas
Assistant Professor

Tutor externo:
Adrià Quintanas Corominas
PhD candidate

Dpto. Mecánica de Medios Continuos y Teoría de Estructuras
Escuela Técnica Superior de Ingeniería
Universidad de Sevilla

Sevilla, 2019

Proyecto Fin de Máster: Coupling of hydrogen assisted embrittlement with a modeling framework for the interaction between the phase field approach for brittle fracture and the interface cohesive zone model

Autor: Ángel de Jesús Valverde González
Tutor y publicador: José Antonio Reinoso Cuevas
Tutor externo: Adrià Quintanas Corominas

El tribunal nombrado para juzgar el trabajo arriba indicado, compuesto por los siguientes profesores:

Presidente:

Vocal/es:

Secretario:

acuerdan otorgarle la calificación de:

El Secretario del Tribunal

Fecha:

Agradecimientos

"Lo que piensas habitualmente determina en gran medida en lo que te convertirás"

— Bruce Lee*, 1940 - 1973*

En primer lugar, quiero agradecer a mi tutor, D. José Antonio Reinoso Cuevas, no solo por su inestimable guía en este proyecto, sino por estos últimos tres años en los que me ha brindado oportunidades que he sabido aprovechar para reforzar mis conocimientos y para poder ir labrándome un futuro en un mundo por el que cada día siento más admiración, que es el de la investigación. Espero y deseo que nuestra colaboración se prolongue en el tiempo lo máximo posible.

Así, también quiero expresar mi gratitud a mi otro tutor, D. Adrià Quintanas Corominas, por la inestimable ayuda que me ha prestado para conseguir sacar adelante el código presentado en este proyecto; y al profesor Israel García García, por su implicación. Muchas gracias, también, a D. Emilio Martínez-Pañeda por su participación, así como, su guía en este proyecto del que espero que obtengamos resultados fructíferos y satisfactorios.

Agradezco además, ya que no tuve oportunidad en su día, a D. Lorenzo García Guzmán, por su magnífica orientación durante mi proyecto de Fin de Grado.

A continuación, quiero dar las gracias a mi familia: a mis padres, Lola y Miguel Ángel; a mi hermano, Rubén; a mis abuelos, Margarita, Miguel, Domingo e Isabel; a mi tío, Francisco; y a mi primo, Alejandro; por haberme apoyado en todos los aspectos tanto profesionales como personales, es decir, por haberme acompañado durante mi etapa de formación así por creer en mí.

Muchas gracias a los amigos que me ha proporcionado la vida, empezando por los que me dejó la carrera, a los cuales cada día más echo de menos tener como compañeros en el día a día. Tampoco me voy a olvidar de mis hermanos de festival, con los que cualquier evento se convierte en una fiesta. A los del camino de Santiago, que no se limitaron a acompañarme únicamente durante lo que duró el trayecto. A mis compañeros de máster, con los que aunque solo hayamos convivido un solo año, hemos forzado lazos que seguro que serán duraderos. También hay sitio para los últimos que han llegado, que son mis jefes y compañeros de trabajo, con los que su afabilidad, cualquier día se hace más llevadero y ameno.

Por último, quiero terminar esta sección dedicándole unas palabras a la persona más importante de mi vida, mi madre: gracias por todo, te quiero mucho.

Ángel de Jesús Valverde González
Máster en Diseño Avanzado en Ingeniería Mecánica

Sevilla, 2019

Resumen

El fenómeno de fragilización de hidrógeno ha sido una causa conocida en procesos de fractura en metales desde el siglo XIX, debido a la degradación en propiedades mecánicas que desencadena la entrada de dicha molécula en el esqueleto del material. Es un caso tan complejo y difícil de analizar que apenas hay referencias de cómo actúa en la estructura interna. Por lo tanto, se hace necesario desarrollar e implementar modelos numéricos que expliquen concretamente cómo de afectada se ve la estructura mecánicamente hablando con la contaminación por hidrógeno, especialmente si se quiere hacer una transición a una economía de hidrógeno limpia y segura.

Por ello, a lo largo del documento, se va a ir desarrollando un código de sólido (*bulk*) e interfase que emplea el modelo matemático de phase field aplicado a mecánica de la fractura y que combina los previamente implementados de D. Emilio Pañeda [1]; y de D. Marco Paggi y de D. José Reinoso [2]; para poder modelizar dicho tipo de corrosión en estructuras metálicas. Para certificar su correcta implementación, además, se presentan ejemplos sobre una placa con una entalla en los que se han discutido la influencia de diversos parámetros y de los que se extrae las posibles aplicaciones que puede tener el modelo desarrollado.

Dichas posibles salidas hablan del posible potencial que tiene, abarcando todo tipo de materiales: desde aceros inoxidables hasta superaleaciones de níquel; diferentes tipos de fractura, ya sea transgranular o intergranular, e incluso, puede valer para implementar el fallo dúctil del sólido.

Abstract

Hydrogen embrittlement phenomenon has been a well-known cause of metal failure and fracture since the 19th century, due to the degradation in mechanical properties that unchains the entrance of this molecule in the material disposition. It is such a complex and difficult case to analyze that there is barely any reference on how it acts in the internal structure. Therefore, there is a real needing for developing and implementing numerical models that explain how specifically gets the structure affected mechanically with respect to hydrogen contamination, specially if a transition to a safe and clean hydrogen economy is desired.

Because of that, throughout the document, a bulk & interface computational framework is going to be developed, which uses the fracture mechanics approach of the mathematical model called phase field and combines the previously implemented ones of Mr. Emilio Pañeda; and of Mr. Marco Paggi and Mr. José Reinoso; to model such type of corrosion on metallic structures. In addition, in order to verify its correct implementation, several examples on a two-grain cracked plate will be presented, discussing the influence of various parameter and extracting from it the possible applications that may represent the developed framework.

Current results pursuit the possible potential that it possess, ranging from all types of materials: from stainless steels to nickel superalloys; different kinds of fracture, such as transgranular or intergranular, and, even, could be of importance to achieve the implementation of ductile fracture in the solid.

Summarized table of contents

Table of contents

Notation

First, the math operators & symbols. Then, greek letters. At last, latin letters.

δ	Differential operator
$\emptyset$	Empty set
$=$	Equal
$\in$	In
$\neq$	Not equal
∂	Partial derivative
$\mathbb{R}^{n_d im}$	Real number field in n dimensions
$\mathbf{1}$	Second order identity tensor
$\nabla_x \bullet$	Spatial gradient operator
$\dot{\bullet}$	Temporal derivative
$tr[\bullet]$	Trace operator
$\bullet^T$	Transpose
α	Grain boundary inclination
χ	Hydrogen damage material coefficient
Δg_b^0	Gibbs free energy difference
$\delta\Omega_C$	Surface with prescribed hydrogen concentration
$\delta\Omega_f$	Surface with prescribed phase field conditions
$\delta\Omega_q$	Surface with prescribed hydrogen flux
$\delta\Omega_t$	Surface with prescribed stresses
$\delta\Omega_u$	Surface with prescribed displacements
$\delta\Omega$	Surface
$\delta\mathscr{W}_e$	External work
$\delta\mathscr{W}_i$	Internal work
$\boldsymbol{\varepsilon}_-$	Strain field (negative values)
$\boldsymbol{\varepsilon}_+$	Strain field (positive values)
ε^i	Strain tensor (eigenvalues)
$\boldsymbol{\varepsilon}$	Strain field
Γ_b	Bulk
Γ_i^{el}	Interface element
Γ_i	Interface
Γ_l	Discrete internal discontinuity
γ	Crack density functional
κ	Residual stiffness
Λ	Specific entropy
λ	Lame's first parameter
η	Lame's second parameter
μ_0	Reference chemical potential
μ	Chemical potential
ν	Poisson's ratio
Ω	Solid

ω	Microstress quantity work (conjugated to ϕ)
$\bar{\phi}$	To-be-averaged phase field parameter
$\hat{\boldsymbol{\phi}}$	Nodal phase field parameter
ϕ	Phase field parameter
Π_{Γ_b}	Potential related to fracture energy in the bulk
$\Pi^{el}_{\Gamma_i}$	Potential related to fracture energy in each element of the interface
Π_{Γ_i}	Potential related to fracture energy in the interface
Π_{Γ}	Potential related to fracture energy
Π_{Ω}	Potential related to elastic energy
Π	Free energy potential
ψ_b	Chemo-elastic stored energy in the bulk
ψ_C	Free chemical energy
ψ_-	Free energy density of the bulk on the damaged state (negative values)
ψ_+	Free energy density of the bulk on the damaged state (positive values)
ψ^e	Elastic energy density
ψ_s	Crack surface energy
$\hat{\psi}$	Total free energy density in the bulk
ψ	Free energy density of the bulk on the damaged state
Σ	Grain boundary notation
$\boldsymbol{\sigma}_0$	Cauchy stress tensor (intact bulk)
$\boldsymbol{\sigma}_-$	Cauchy stress tensor (compressive values)
$\boldsymbol{\sigma}_+$	Cauchy stress tensor (tensile values)
σ_c	Normal traction component (interface, critical value)
σ_H	Hydrostatic stress tensor
$\boldsymbol{\sigma}$	Cauchy stress tensor
σ	Normal traction component (interface)
τ_c	Tangential traction component (interface, critical value)
τ	Tangential traction component (interface)
Θ	Absolute temperature
θ_H	Hydrogen coverage
θ_L	Lattice sites occupancy
$\boldsymbol{\xi}$	Microstress quantity work (conjugated to $\nabla\phi$)
$\boldsymbol{B}_{\phi}$	Phase field compatibility operator
$\boldsymbol{B}_{\boldsymbol{C}}$	Hydrogen concentration compatibility operator
$\boldsymbol{B}_{\boldsymbol{u}}$	Displacements compatibility operator (standard strain matrices)
$\boldsymbol{C}_{\mathbf{0}}$	Linear elastic stiffness matrix
C_0	Reference lattice hydrogen concentration
$C_{b,left}$	Left grain surfacing hydrogen concentration
$C_{b,right}$	Right grain surfacing hydrogen concentration
C_b	Surfacing hydrogen concentration
$CPE4$	4-node plane strain full scheme integration element
$CPE8R$	8-node plane strain reduced scheme integration element
CZM	Cohesive zone model
$\mathbb{C}$	Tangent constitutive operators
$\hat{\boldsymbol{C}}$	Nodal hydrogen concentration
$\bar{C}$	To-be-averaged hydrogen concentration
C	Hydrogen concentration
$\frac{da}{dt}$	Crack growth
DFT	Density functional theory
D	Diffusion coefficient
$\mathscr{E}$	Specific internal energy
E	Young Modulus

e	Number e
FEAP	Finite Element Analysis Program
FEM	Finite Element Method
$\boldsymbol{F_i}$	Diffusion flux factor
F_{mx}	Maximum force
$\boldsymbol{f_v}$	Body force field per volume
f	Microtraction
$\mathscr{G}_C^b$	Fracture bulk energy
$\mathscr{G}_C$	Fracture energy
$\mathscr{G}_{C,left}^b$	Left grain critical energy release rate (bulk)
$\mathscr{G}_{C,right}^b$	Right grain critical energy release rate (bulk)
$\mathscr{G}_I^i$	Mode I energy release rate (interface)
$\mathscr{G}_{II}^i$	Mode II energy release rate (interface)
$\mathscr{G}_{IC}^i$	Mode I critical energy release rate (interface)
$\mathscr{G}_{IIC}^i$	Mode II critical energy release rate (interface)
$\mathscr{G}^i$	Fracture interface energy
$\boldsymbol{g}_{loc}$	Local gap
$g_{nc,0}$	Critical interface displacement normal gap (intact state)
$g_{nc,1}$	Critical interface displacement normal gap (fully broken state)
g_{nc}	Critical interface displacement normal gap
g_n	Normal interface displacement gap
$g_{tc,0}$	Critical interface displacement tangential gap (intact state)
$g_{tc,1}$	Critical interface displacement tangential gap (fully broken state)
g_{tc}	Critical interface displacement tangential gap
g_t	Tangential interface displacement gap
$\boldsymbol{g}$	Interface displacement gaps field
g	Degradation function
H_2	Hydrogen molecule
HE	Hydrogen embrittlement
H_t	Energy at increment
H	Hydrogen atomic symbol
H	History variable field
h	Characteristic element size
$\boldsymbol{J}$	Hydrogen flux
k_n	Normal interface stiffness
$\boldsymbol{K}^{\phi\phi}$	Phase field-phase field stiffness matrix
$\boldsymbol{K}^{\phi\boldsymbol{u}}$	Phase field-displacement stiffness matrix
$\boldsymbol{K}^{CC}$	Hydrogen concentration-hydrogen concentration stiffness matrix
$\boldsymbol{K}^{\boldsymbol{u}\phi}$	Displacement-phase field stiffness matrix
$\boldsymbol{K}^{\boldsymbol{uu}}$	Displacement-displacement stiffness matrix
kJ	kiloJoule
$k_{n,0}$	Normal interface stiffness (intact state)
k_n	Normal interface stiffness
$k_{t,0}$	Tangential interface stiffness (intact state)
k_t	Tangential interface stiffness
K	Bulk modulus / Kelvin
LEFM	Linear elastic fracture mechanics
$\boldsymbol{L}$	Matrix operator
ℓ	Length scale parameter
$\boldsymbol{M}_\phi$	Average phase field operator
$\boldsymbol{M}_C$	Average hydrogen concentration operator
Mg	Magnesium
$\boldsymbol{M}_{ij}$	Concentration capacity matrix
mm	Milimeter

MPa	MegaPascal
$\boldsymbol{N}_{\phi}$	Phase field interpolation matrix
$\boldsymbol{N}_{C}$	Hydrogen concentration interpolation matrix
$\boldsymbol{N}_{i}$	Interpolation matrix
N_{i}	Nodal shape function
$\boldsymbol{n}^{i}$	Strain tensor (eigenvectors)
Ni	Nickel
$\boldsymbol{N}_{u}$	Displacement field interpolation matrix
N	Lattice sites
N	Newton
$\boldsymbol{n}$	Outward normal
q	Concentration flux
ppm	Parts-per-million
$\boldsymbol{Q}$	Heat flux
Q	Heat absorption
r^{ϕ}	Phase field residual
r^{C}	Hydrogen concentration residual
$\boldsymbol{r}^{u}$	Displacement residuals
$\boldsymbol{R}$	Rotation matrix
R	Universal gas constant
t_{f}	Final testing pseudo-time
T	Temperature
t	Time
$\hat{\boldsymbol{u}}$	Nodal displacements
$\boldsymbol{u_x}$	Horizontal displacements
$\boldsymbol{u_y}$	Vertical displacements
$\boldsymbol{u}$	Displacement field
$\bar{V}_{H}$	Partial molar volume of hydrogen in solid solution
wt	Weight
x_{c}	Position parameter in the interface
$\boldsymbol{x}$	Vector of position
x	Position parameter

1 Introduction

Hydrogen Embrittlement (HE) has been known to be a cause of fracture in metals since the 19th century [3] [4]. This phenomena consists of a dangerous and unpredictable degradation of properties caused by the presence of gaseous H_2 in the local environment [5]. Hydrogen atoms are absorbed into the material, diffuse through the lattice to be accumulated in particular sites (such as grain boundaries, as can be seen in fig. 1.1) and therefore, they induce fracture [6]. It is only necessary a small amount of atomic H at the ppm level to drastically reduce ductility and strength of the metallic lattice. Furthermore, HE may initiate and propagate subcritical cracks, occurring the event of fast fracture after the crack reaches a critical length, which leads to sudden failure. An example of the importance of this catastrophic fracture aspect is reflected in events such as the collapse of a concrete roof in a Swiss indoor swimming pool in 1985, which killed 12 people [7].

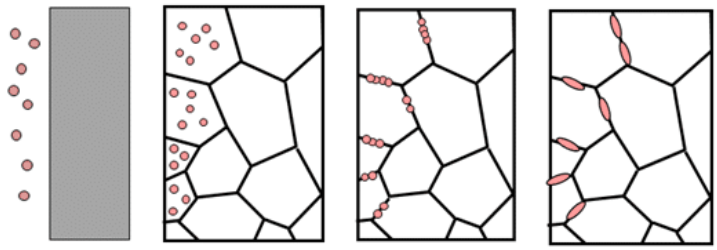

Figure 1.1 Hydrogen embrittlement: mechanism of entrance [6].

HE affects to a range of metals, like stainless steels [5] [8] [9], Mg alloys [10] [11], Ni alloys [12] [13], Inconel alloys [14], etc. Therefore, it is a expanded problem for many metallic materials. However, despite extensive studies in literature, the micro-mechanisms governing HE are not fully understood because of its complexity and the found difficulties for experimentation. Proof of that is in the absence of a database on the mechanical response of steels affected by HE [15]. Such kind of database is essential to design large durability components in the so-called hydrogen economy, especially in the manufacturing, transport, and energy industries. Hence, there is a strong need to understand, quantify, and model how hydrogen affects the resistance of metals inducing fracture and reducing its durability [1].

Modelling efforts in the hydrogen embrittlement community have been developed eminently via discrete numerical methods. The process of crack initiation and growth has been computed with dislocation-based models [16], weakest-link methods [17] [18] and mainly, cohesive approaches [19] [20], being this last group one of the main focus in this work.

The cohesive elements modeling technique consists of using an interface whose response is characterized by a traction-separation law [21]. This proportionate a versatile framework. For instance, regarding to the modeling of the HE phenomena, strength reduction caused by an increase of the hydrogen concentration can be easily incorporated in the traction-separation law. On the other hand, the principal drawback of the cohesive elements when modeling interfaces is the inability of modeling complex crack patterns, such as the ones concerning branching phenomena.

Cohesive models display a solid performance in situations the integrity and strength of interfaces are of interest. The importance of interfaces may be observed, for instance, in biologic systems, ranging from human bone [22] to sea shell [23], which show combinations of mechanical properties (e.g. deformability,

strength and toughness at the same time) which are not conceived in engineering materials. In fact, as they do not show anything comparable to metals at their disposal (for instance, they do not show the movement and generation of dislocations), these aspects rely on their inherent morphology, based on hard and strong blocks joined by interfaces [24].

When studying fracture mechanics of complex configurations, interfaces have an essential role as potential deflecting channels for cracks. This, in turn, may induce toughening phenomena, enabling the structure to reach larger deformations [25]. In addition to this, they favor deformed hardening in order to spread dissipative energy mechanisms throughout the whole solid of the material [26] [27]. For the previous reasons, this toughening phenomena induced by the crack deflection has been a source of inspiration for researchers to develop a new type of materials with better mechanical properties.

Differing from previous approaches, a promising variational framework called phase field has emerged to overcome the limitations of the current fracture models. The foundations of phase-field approaches for brittle fracture are related to the classic thermodynamical Griffith's criterion, introducing a total energy functional that is the addition of the fracture and elastic energy. The minimization of this functional allows triggering crack nucleation, propagation and coalescence in the continuum [2]. This method has gained notice since the early works by Francfort, Marigo [28] & Bourdin [29] [30]; and important efforts have been developed by Miehe et al. to improve solution schemes [31] and by Borden, to discretization strategies [32]. In addition, it has been extended to model ductile fracture [33], multi-physics approaches [34] [35], composite delamination [36] [37] [38], among other cases.

In the present study, two different computational frameworks will be analyzed and subsequently developed. The first one is the implemented formulation for hydrogen assisted cracking employing the phase-field method by Martínez-Pañeda [1]. In this research, the phase field framework employed for a sharp crack is combined with the degradation of the surface energy caused by the hydrogen coverage, which diffuses (driven by chemical potential gradients) through the solid and causes the fracture energy to decrease. This coupled problem is solved with a implicit time integration scheme, employing finite element method, where displacements, phase field order parameter and hydrogen concentration are the primary variables. Computations reveal a notable compability with the results from the experiments, proving that the formulations for fracture are suitable in order to acquire material degradation caused by hydrogen.

The other research line related to this work consists of a modeling framework which combines a phase-field model for brittle fracture in the bulk with a cohesive one modeled for a pre-existing interface, which is made to be fully compatible for the phase-field approach, developed by Paggi and Reinoso [2]. Implemented via finite element analysis program FEAP [39] with a monolithic fully implicit solucion scheme, the robustness of this model is put into test with various instances related to the crack propagation, obtaining results with a good agreement with linear elastic fracture mechanics (LEFM) predictions in homogeneus systems for the classical problem of competition between deflection and penetration. After proving its accuracy, it is used to offer plausible explanations with regard to previous experiments [40] [41] for the meeting of a crack perpendicularly in a bi-material interface (fig. 1.2), a problem not available analitically.

Both approaches for hydrogen embrittlement, on one side, and brittle fracture and interface cohesive zone model (CZM), on the other side, will be coupled in order to develop a phase-field framework in the bulk and interface of a two solids system, which will be verified by its application to different mechanical instances. The main target of this research is to analyze how hydrogen coverage affects both bulk and interface fracture energy.

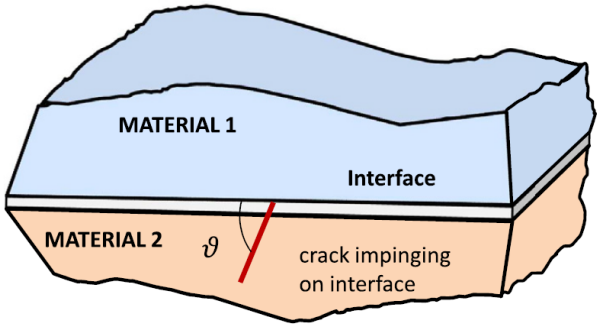

Figure 1.2 Crack at a bi-material interface, one of the problems where [2] was successfully implemented.

2 Theoretical formulation

The numerical scheme of this chapter is grounded on: i) introduction, ii) phase field approach for brittle fracture in the bulk, iii) phase field coupling with CZM for interface delamination, iv) surface energy degradation dependence on the hydrogen coverage.

2.1 Introduction

The so-called phase field fracture method is based on the variational approach of brittle fracture governing of nucleation, propagation and branching, which is set-up by the definition of the following free energy functional [42] [43]:

$$\Pi(\boldsymbol{u},\Gamma) = \Pi_{\Omega}(\boldsymbol{u},\Gamma) + \Pi_{\Gamma}(\Gamma) = \int_{\Omega/\Gamma} \psi^{e}(\boldsymbol{\varepsilon})\mathrm{d}\Omega + \int_{\Gamma} \mathscr{G}_{C}\mathrm{d}\Gamma \tag{2.1}$$

where $\psi^{e}(\boldsymbol{\varepsilon})$ stands for the elastic energy density dependent upon the strain field $\boldsymbol{\varepsilon}$ and $\mathscr{G}_{C}$ is the fracture energy. It is seen that there are two different terms in eq. 2.1, being $\Pi_{\Omega}(\boldsymbol{u},\Gamma)$ the one that represents the elastic energy stored in the solid and $\Pi_{\Gamma}(\Gamma)$, the energy necessary to create the crack according to Griffith theory.

The main idea of this framework for its application to heterogeneous media with prescribed interfaces relies on the split of the fracture energy in two parts, one correspondent to the dissipated energy in the bulk Ω and the other, along the interface Γ. This decomposition renders

$$\Pi_{\Gamma} = \Pi_{\Gamma_b} + \Pi_{\Gamma_i} = \int_{\Gamma_b} \mathscr{G}_{C}^{b}(\boldsymbol{u},\phi)\mathrm{d}\Gamma + \int_{\Gamma_i} \mathscr{G}^{i}(\boldsymbol{u},\phi)\mathrm{d}\Gamma \tag{2.2}$$

The bulk energy $\mathscr{G}_{C}^{b}$ is dissipated according to the Griffith theory [44] and the interface energy $\mathscr{G}^{i}$, according to the cohesive zone formulation. In fact, it will be considered that the interface is ruled via a traction-separation law with a simple tension cut-off [2].

In fact, this interface dissipation energy factor $\mathscr{G}^{i}$ is related to the displacement discontinuities in the interface $\boldsymbol{g}$, a history parameter H, as it is stated in [45], and to the phase field parameter ϕ.

$$\mathscr{G}^{i} = \mathscr{G}^{i}(\boldsymbol{g},H,\phi) \tag{2.3}$$

Therefore, based on this assumptions, eq. 2.1 may be rewritten as:

$$\Pi(\boldsymbol{u},\Gamma_b,\Gamma_i) = \Pi_{\Omega} + \Pi_{\Gamma_b} + \Pi_{\Gamma_i} = \int_{\Omega/\Gamma} \psi^{e}(\boldsymbol{\varepsilon})\mathrm{d}\Omega + \int_{\Gamma_b} \mathscr{G}_{C}^{b}(\boldsymbol{u},\phi)\mathrm{d}\Gamma + \int_{\Gamma_i} \mathscr{G}^{i}(\boldsymbol{u},\phi)\mathrm{d}\Gamma \tag{2.4}$$

where the bulk functional $\Pi_{b}(\boldsymbol{u},\Gamma_b)$ is:

$$\Pi_{b}(\boldsymbol{u},\Gamma_b) = \Pi_{\Omega} + \Pi_{\Gamma_b} = \int_{\Omega/\Gamma} \psi^{e}(\boldsymbol{\varepsilon})\mathrm{d}\Omega + \int_{\Gamma_b} \mathscr{G}_{C}^{b}(\boldsymbol{u},\phi)\mathrm{d}\Gamma \tag{2.5}$$

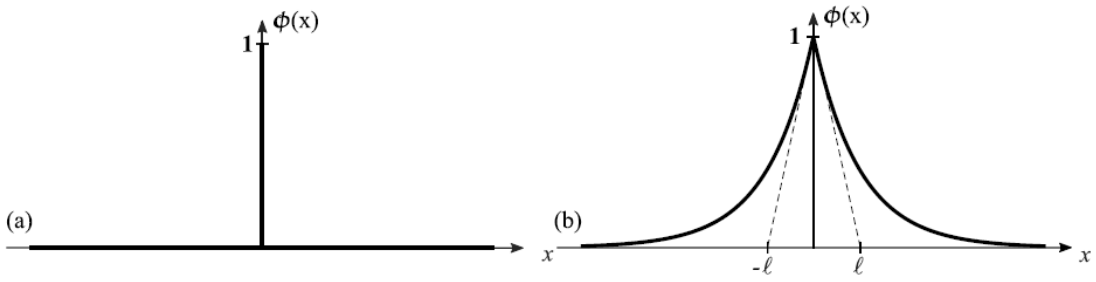

Figure 2.1 Sharp and diffusive crack topology. a) Sharp crack at x= 0. b) Diffusive crack at x= 0 modeled with the crack parameter of phase field ϕ, dependent on the length ℓ [1].

2.2 Phase field approach for brittle fracture in the bulk

In a one-dimensional setting, the topology of a sharp crack (see. fig. 2.1a) may be described by the phase field parameter $\phi(x) \in [0,1]$, with

$$\phi(x) = \begin{cases} 1 & \text{if } x = 0 \\ 0 & \text{if } x \neq 0 \end{cases} \tag{2.6}$$

with $\phi = 0$ and $\phi = 1$ respectively denoting the intact and fractured states of the solid.

On the other hand, the diffusive crack modeled by phase field (see. fig. 2.1b) may be approached by the function:

$$\phi(x) = e^{-\frac{|x|}{\ell}} \tag{2.7}$$

The length scale parameter ℓ represents the width of the smearing function, approaching the sharp topology at $\ell \to 0$.

With these approaches, the potential energy of the system is decomposed into two terms [42] [46]:

$$\Pi_{\Gamma_b}(\boldsymbol{u},\phi) = \int_\Omega \psi(\boldsymbol{\varepsilon},\phi)\mathrm{d}\Omega + \int_\Omega \mathscr{G}_C^b \gamma(\phi,\nabla_x\phi)\mathrm{d}\Omega \tag{2.8}$$

where $\psi(\boldsymbol{\varepsilon},\phi)$ stands for the energy density of the bulk on the damaged state and $\gamma(\phi,\nabla_x\phi)$, as the crack density functional, with $\nabla_x\bullet$ the spatial gradient operator. The total free energy density of the bulk $\hat{\psi}$ may be read as:

$$\hat{\psi} = \psi(\boldsymbol{\varepsilon},\phi) + \mathscr{G}_C^b \gamma(\phi,\nabla_x\phi) \tag{2.9}$$

Focusing first on the energy density of the bulk, $\psi(\boldsymbol{\varepsilon},\phi)$, the following partition in positive and negative is put forward [47]:

$$\psi(\boldsymbol{\varepsilon},\phi) = g(\phi)\psi_+(\boldsymbol{\varepsilon}) + \psi_-(\boldsymbol{\varepsilon}) \tag{2.10}$$

$$\psi_+(\boldsymbol{\varepsilon}) = \frac{\lambda}{2}(\langle tr[\boldsymbol{\varepsilon}]\rangle_+)^2 + \eta tr[\boldsymbol{\varepsilon}_+^2] \tag{2.11}$$

$$\psi_-(\boldsymbol{\varepsilon}) = \frac{\lambda}{2}(\langle tr[\boldsymbol{\varepsilon}]\rangle_-)^2 + \eta tr[\boldsymbol{\varepsilon}_-^2] \tag{2.12}$$

where λ and η denote the Lamé constants; $tr[\bullet]$, the trace operator and $g(\phi)$, the phase field degradation function, which takes the function:

$$g(\phi) = (1-\phi)^2 + \kappa \tag{2.13}$$

being κ a parameter of residual stiffness which avoids the system from becoming ill-conditioned and numerical instabilities.

The decomposition of the strain tensor in eqs. 2.11-2.12 in positive and negative counterparts is made in order to account the damage only under tensile conditions: $\boldsymbol{\varepsilon} = \boldsymbol{\varepsilon}_+ + \boldsymbol{\varepsilon}_-$. The spectral decomposition of the positive part of the strain tensor reads

$$\boldsymbol{\varepsilon}_+ = \sum_{i=1}^{n_{dim}} \langle \varepsilon^i \rangle_+ \boldsymbol{n}_\varepsilon^i \otimes \boldsymbol{n}_\varepsilon^i \tag{2.14}$$

where ε^i and $\boldsymbol{n}^i$ represent the eigenvalues and eigenvectors of the strain tensor and $\langle \bullet \rangle_+ = \frac{\bullet + |\bullet|}{2}$.

According to [48], relying on standard arguments, the Cauchy stress tensor $\boldsymbol{\sigma}$ may be defined by:

$$\boldsymbol{\sigma} := \frac{\partial \hat{\psi}}{\partial \boldsymbol{\varepsilon}} = g(\phi)\boldsymbol{\sigma}_+ + \boldsymbol{\sigma}- \tag{2.15}$$

with $\boldsymbol{\sigma}_\pm = \lambda(\langle tr[\boldsymbol{\varepsilon}] \rangle_\pm)\mathbf{1} + 2\eta\boldsymbol{\varepsilon}_\pm$, where $\mathbf{1}$ denotes the second order identity tensor.

Irreversibility of the fracture process is guaranteed with the addition of a penalty term related to the local damage history [42] [49]. Said thermodynamic consistency based on the Clausius-Planck inequality has been fully addressed in [42].

On the other hand, about the crack density functional, Miehe et al. [42] states that $\gamma(\phi, \nabla_x\phi)$ is a convex functional composed by two quadratic terms: one for the phase field parameter ϕ and the other related to its gradient $\nabla_x\phi$. This functional is read

$$\gamma(\phi, \nabla_x\phi) = \frac{1}{2\ell}\phi^2 + \frac{\ell}{2}|\nabla_x\phi|^2 \tag{2.16}$$

Therefore, the corresponding Euler equations associated with the phase field problem take the form:

$$\phi - \ell^2\nabla_x^2\phi = 0 \; in \; \Omega \tag{2.17}$$

$$\nabla_x\phi \cdot \boldsymbol{n} = 0 \; in \; \delta\Omega \tag{2.18}$$

where $\nabla_x^2\phi$ denotes the Laplacian of the phase field parameter.

Through the insertion of both detailed terms into eq. 2.8, one obtains:

$$\Pi_{\Gamma_b}(\boldsymbol{u}, \phi) = \int_\Omega \left[[(1-\phi)^2 + \kappa]\psi_+^e + \mathscr{G}_C\left(\frac{1}{2\ell}\phi^2 + \frac{\ell}{2}|\nabla_x\phi|^2\right)\right] d\Omega \tag{2.19}$$

Correspondingly, the weak form of the variational problem associated with the bulk fracture renders

$$\delta\Pi_{\Gamma_b}(\boldsymbol{u}, \delta\boldsymbol{u}, \phi, \delta\phi) = \int_\Omega \left[-2(1-\phi)\delta\phi\,\psi_+^e + \mathscr{G}_C\left(\frac{1}{\ell}\phi\,\delta\phi + \ell\nabla_x\phi \cdot \nabla_x(\delta\phi)\right)\right] d\Omega \tag{2.20}$$

At last, if the product rule and Gauss'divergence theory are applied, phase field equilibrium equation is obtained:

$$\mathscr{G}_C\left(\frac{1}{\ell}\phi - \ell\Delta\phi\right) - 2(1-\phi)\psi_0^e = 0 \tag{2.21}$$

2.3 Phase field coupling with CZM for interface delamination

The interface fracture energy potential introduced in eq. 2.4 is divided into the sum of the Mode I and Mode II energy release rates, $\mathscr{G}_I$ and $\mathscr{G}_{II}$, based on the considered CZM. As it was stated in section 2.1, a linear Mode I and Mode II traction-separation law with tension cut-off upon failure is adopted, with previous applications studied in [50] [51] [52].

In order to propose a formulation as general as possible, the postulation of the CZM description on the phase field developed by Paggi and Reinoso in [2] is herein advocated. In this environment, displacement jump $\boldsymbol{g}$ is considered a function of the phase field parameter ϕ that produces fracture phenomena in the contigous continuum body. A linear dependency among those variables is proposed. Hence, critical displacement gap may be increased or reduced basing on the values of ϕ, which range from zero to one. This first scenario is representative of structured biological interfaces, commentated above in section 1, while the latter is related to damaged interfaces induced by the increasing of damage in the interface material [53].

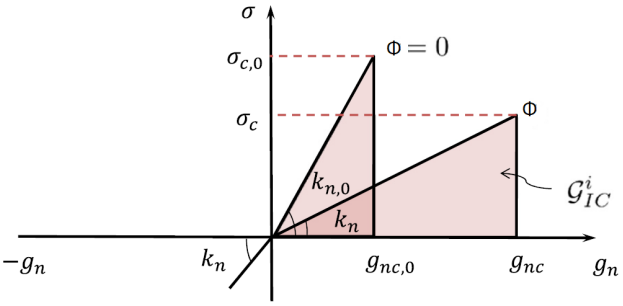

Figure 2.2 Representation of the CZM coupled with the phase field variable ϕ for brittle fracture in the interface. Mode I CZM traction σ vs. g_n [2].

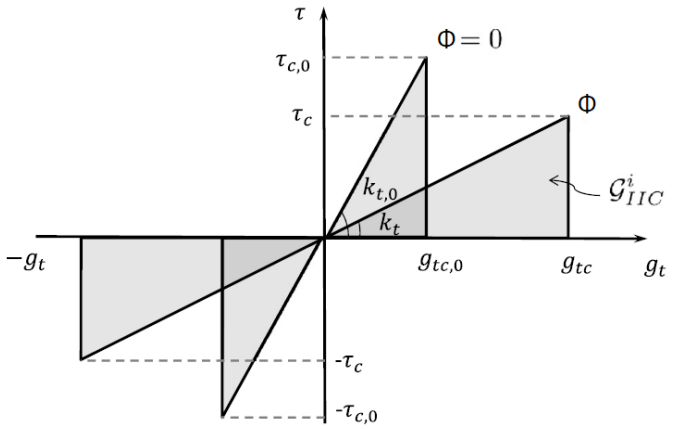

Figure 2.3 Representation of the CZM coupled with the phase field variable ϕ for brittle fracture in the interface. Mode II CZM traction τ vs. g_t [2].

Recalling the approach, it is worth noting that it assumes that there is no variation with respect to the energy dissipation depending on the characteristic properties of the interface. Therefore, in the previous scenarios the interface fracture energy remains constant with respect to ϕ. Then, in Mode I, an increasing in the critical normal displacement gap g_{nc} by the increasing of the phase field parameter ϕ causes a simultaneous reaction in the stiffness k_n and in the critical traction σ_c. Same behaviour occurs in Mode II (see figs. 2.2 & 2.3).

In order to state a linear relation among the Mode I critical displacement normal gap g_{nc} and the phase field parameter ϕ, the following equation is defined:

$$g_{nc}(\phi) = (1-\phi)g_{nc,0} + \phi g_{nc,1} \tag{2.22}$$

where $g_{nc,0} = g_{nc}(\phi = 0)$ and $g_{nc,1} = g_{nc}(\phi = 1)$. Therefore, for the Mode I cohesive traction it is deduced:

$$\sigma = \begin{cases} k_n \frac{g_n}{g_{nc}} & \text{if } 0 \leq \frac{g_n}{g_{nc}} \leq 1 \\ 0 & \text{if } \frac{g_n}{g_{nc}} \geq 1 \end{cases} \tag{2.23}$$

where σ denotes the normal traction component of the interface, being σ_c the critical value.

The corresponding Mode I interface fracture energy $\mathscr{G}^i_{IC}$ reads

$$\mathscr{G}^i_{IC} = \frac{1}{2} k_n g_{nc}^2 \tag{2.24}$$

By imposing the condition that $\mathscr{G}^i_{IC}$ is independent from ϕ, the expression por k_n is obtained by equating the generic value of the interface fracture energy $\mathscr{G}^i_{IC}$ to the value correspondent to the intact bulk ($\phi = 0$).

$$k_n = k_{n,0} \left(\frac{g_{nc,0}}{g_{nc}} \right)^2 \tag{2.25}$$

where $k_{n,0}$ stands for the interface stiffness for the intact solid. Taking into account this last expression, the one for Mode I energy release rate is herein deduced:

$$\mathscr{G}_I^i(\phi) = \frac{1}{2} k_{n,0} g_n^2 \frac{g_{nc,0}^2}{[(1-\phi) g_{nc,0} + \phi g_{nc,1}]^2} \tag{2.26}$$

Same functional expressions may be proposed for Mode II. First, a linear relation between the Mode I critical displacement sliding gap g_{tc} and the phase field parameter ϕ is proposed:

$$g_{tc}(\phi) = (1-\phi) g_{tc,0} + \phi g_{tc,1} \tag{2.27}$$

where $g_{tc,0} = g_{tc}(\phi = 0)$ and $g_{tc,1} = g_{tc}(\phi = 1)$. Herein, for the Mode II cohesive traction it is deduced:

$$\tau = \begin{cases} k_t \frac{g_t}{g_{tc}} & \text{if } 0 \leq \frac{g_t}{g_{tc}} \leq 1 \\ 0 & \text{if } \frac{g_t}{g_{tc}} \geq 1 \end{cases} \tag{2.28}$$

where τ denotes the sliding traction component of the interface, being τ_c the critical value.

The corresponding Mode II interface fracture energy reads as:

$$\mathscr{G}_{IIC}^i = \frac{1}{2} k_t g_{tc}^2 \tag{2.29}$$

In order to provide a Mode II interface fracture energy $\mathscr{G}_{IIC}^i$ independent of ϕ, the stiffness k_t of the traction-sliding equating satisfies the following condition:

$$k_t = k_{t,0} \left(\frac{g_{tc,0}}{g_{tc}} \right)^2 \tag{2.30}$$

And, therefore, the Mode II energy release rate is defined as:

$$\mathscr{G}_{II}^i(\phi) = \frac{1}{2} k_{t,0} g_t^2 \frac{g_{tc,0}^2}{[(1-\phi) g_{tc,0} + \phi g_{tc,1}]^2} \tag{2.31}$$

At last, in order to treat Mixed Mode conditions, a quadratic criterion is herein adopted:

$$\left(\frac{\mathscr{G}_I^i}{\mathscr{G}_{IC}^i} \right)^2 + \left(\frac{\mathscr{G}_{II}^i}{\mathscr{G}_{IIC}^i} \right)^2 = 1 \tag{2.32}$$

where

$$\mathscr{G}_{IC}^i = \frac{1}{2} k_{n,0} g_{nc,0}^2; \quad \mathscr{G}_{IIC}^i = \frac{1}{2} k_{t,0} g_{tc,0}^2; \tag{2.33}$$

Regarding back to the interface contribution to the functional of the system corresponding to the term Π_{Γ_i} in eq. 2.4, its virtual variation may be read as:

$$\delta \Pi_{\Gamma_i} = \int_{\Gamma_i} \left(\frac{\partial \mathscr{G}^i(\boldsymbol{u}, \phi)}{\partial \boldsymbol{u}} \delta \boldsymbol{u} + \frac{\partial \mathscr{G}^i(\boldsymbol{u}, \phi)}{\partial \phi} \delta \phi \right) \mathrm{d}\Gamma \tag{2.34}$$

2.4 Surface energy degradation dependence on the hydrogen coverage

As stated in Chapter 1, hydrogen enters the material and reduces its fracture resistance. Its mechanism consists in a weakening of the bonds between metal atoms by lowering bonding energy. Several authors have employed Density Functional Theory (DFT) in order to research the decohesion of fracture surfaces with the variation of hydrogen coverage, such as [54] [55].

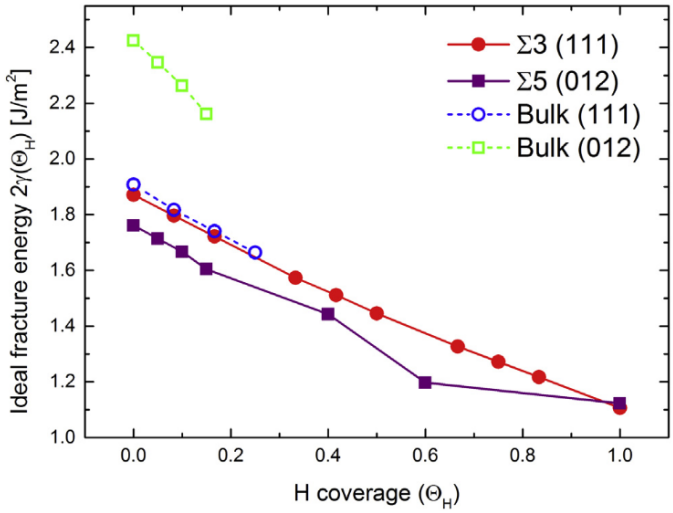

Figure 2.4 Effect of hydrogen coverage on the surface energy of nickel in the bulk and grain boundaries [55].

For example, Alvaro et al. [55] observed the variation in ideal fracture energy by the presence of hydrogen atoms at Σ3 and Σ5 grain boundaries in nickel, along with different planes in the bulk. Fig. 2.4 shows the surface energy - hydrogen coverage curves obtained by their studies .

Table 2.1 Measuring factor χ for different materials, obtained via first principles quantum mechanics..

Material	Damage coefficient χ	DFT analysis
Nickel	0.41	Alvaro et al. [55]
Aluminium	0.67	Jiang et Carter. [54]
Iron	0.89	Jiang et Carter. [54]

One may define the relation among critical energy release rate $\mathscr{G}_C^i$ with the hydrogen coverage θ_H may as:

$$\frac{\mathscr{G}_C^i(\theta_H)}{\mathscr{G}_C^i(0)} = 1 - \chi\theta_H \tag{2.35}$$

where $\mathscr{G}_C^i(0)$ denotes the critical energy release rate in absence of hydrogen and χ, the damage coefficient dependent of the the material that measures the lowering of the fracture hydrogen caused by the hydrogen coverage θ_H. χ for iron, aluminium and nickel is displayed in table 2.1, along with the authors who analyzed them.

Direct effect of hydrogen coverage θ_H on the fracture resistance may be illustrated by analyzing analytical homogeneous solutions of a 1-D quasi-static problem. Because of that, the Cauchy stress tensor $\boldsymbol{\sigma}$ is given by:

$$\boldsymbol{\sigma} = g(\phi)E\boldsymbol{\varepsilon} \tag{2.36}$$

where E denotes the Young modulus and $\boldsymbol{\varepsilon}$ the strain tensor.

If a strain energy density $\psi_0^e = \frac{E\boldsymbol{\varepsilon}^2}{2}$ is given, one can readily obtain the homogeneous phase field from the strong form, eq. 2.21.

$$\phi = \frac{E\boldsymbol{\varepsilon}^2\ell}{\mathscr{G}_C^i + E\boldsymbol{\varepsilon}^2\ell} \tag{2.37}$$

Whether this relation is substituted into the following constitutive equation, relating the strain and stress states; it is obtained:

$$\boldsymbol{\sigma} = \left(\frac{E\boldsymbol{\varepsilon}^2\ell}{\mathscr{G}_C^i + E\boldsymbol{\varepsilon}^2\ell}\right)^2 E\boldsymbol{\varepsilon} \tag{2.38}$$

From the previous constituvie equation, the critical stress quantity σ_C is obtained by:

$$\sigma_C = \sqrt{\frac{27E\mathscr{G}_C^i}{256\ell}} \tag{2.39}$$

as well as the maximum strain counterpart ε_C:

$$\varepsilon_C = \sqrt{\frac{\mathscr{G}_C^i}{3E\ell}} \tag{2.40}$$

Steming from the previous relationships, the phase field regularisation length ℓ can be considered a material parameter [56], as it governs the magnitude of the critical stress & strain at which damage initiates. This fact implies that the value of the critical energy release rate $\mathscr{G}_C^i$ is strongly related to the choice of ℓ, obtaining the Griffith's value for $\ell \to 0$. From the eq. 2.38, an analogy with cohesive zone frameworks is established. Having this in mind, the characteristic element size h in cohesive analyses is typically selected to be [57] [58]:

$$h < \frac{\pi}{160}\frac{E\mathscr{G}_C^i}{\sigma_C^2} \tag{2.41}$$

Finally, the Langmuir-McLean isotherm is used to compute the surface coverage θ_H from the bulk hydrogen concentration C:

$$\theta_H = \frac{C}{C + exp\left(\frac{-\Delta g_b^0}{RT}\right)} \tag{2.42}$$

with C being given in units of impurity mole fraction and R is the universal gas constant; T, the temperature; and Δg_b^0, the Gibbs free energy difference among the interface and the surrounding material. The present formulation guarantees the effect of microstructural traps on cracking and is able to incorporate mass transport fenomena through an effective diffusion value.

As illustrated in fig. 2.5, the increase of the hydrogen concentration reduces significally the strength and fracture resistance for iron-based materials ($\chi = 0.89$). Current framework studies the sensitivity of surface energy to hydrogen coverage, even though that other mechanisms of hydrogen damage may also be added.

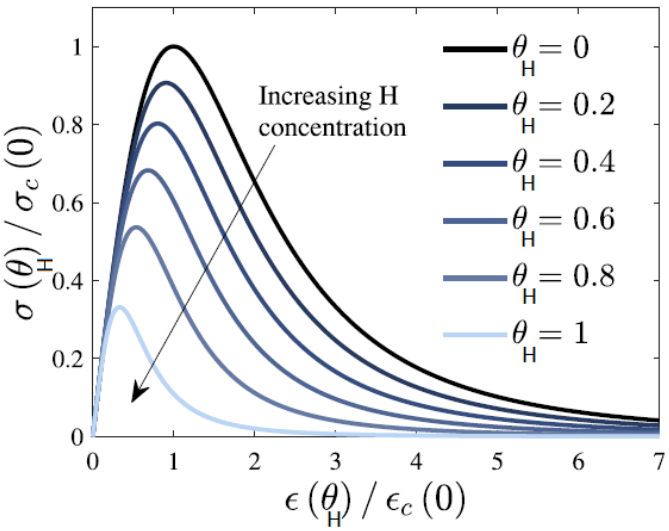

Figure 2.5 Dependence of hydrogen coverage θ_H on the damage constitutive law for iron-based materials. There is a normalization by employing $\theta_H = 0$ [1].

The above information is related to the effect of hydrogen coverage θ_H to the bulk energy release rate. In order to relate interface energy with θ_H, eqs. 2.33 & 2.35 will be both combined to obtain a expression for

both critical energy release rates which depend on hydrogen concentration

$$\mathscr{G}_{IC}^{i} = \frac{1}{2} k_{n,0} g_{nc,0}^{2} (1 - \chi \theta_H); \quad \mathscr{G}_{IIC}^{i} = \frac{1}{2} k_{t,0} g_{tc,0}^{2} (1 - \chi \theta_H); \tag{2.43}$$

In order to quantify how is the effect of hydrogen coverage θ_H to both critical energy release rates, an analytical study about the dependence of the curve σ/τ vs. normal/tangential critical displacement (see figs. 2.2 & 2.3) on the hydrogen concentration C (which is directly related to θ_H, see eq. 2.42) has been put forward in fig. 2.6. As it can be seen in such figure, both critical displacements and stresses (and therefore, the critical energy release rates) are severely reduced, even at low hydrogen concentrations. In fact, it is derived from such study that when this concentration increases, the decrease of such parameters is weaken.

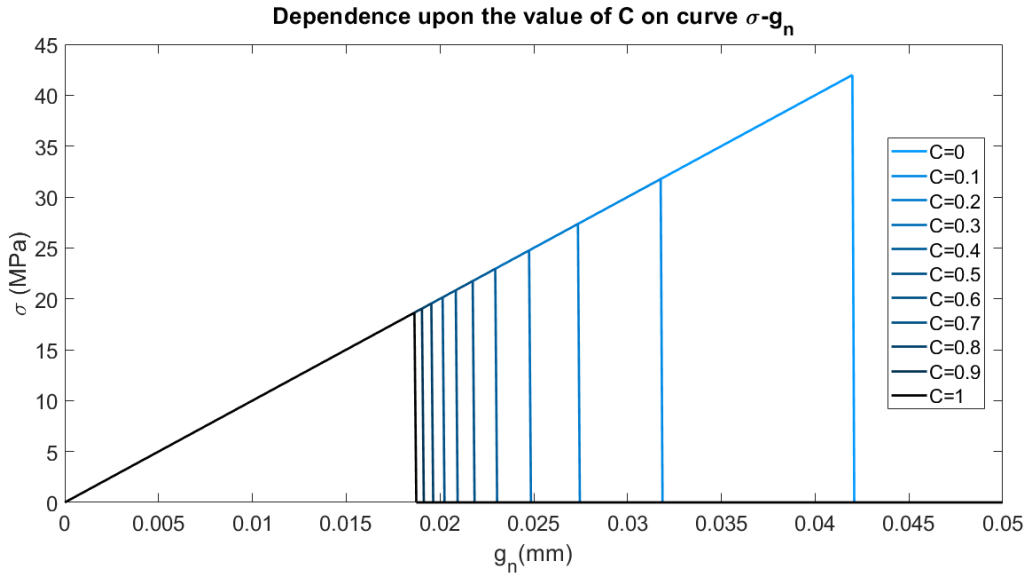

Figure 2.6 Effect of hydrogen concentration C on the curve σ vs. normal critical displacement. Same behaviour happens with τ vs. tangential critical displacement.

3 Numerical formulation & FE implementation

The numerical scheme of this chapter is grounded on: i) initial hypothesis, ii) numerical implementation in the bulk, iii) numerical implementation in the interface.

3.1 Initial hypothesis

First of all, it is necessary to establish the initial hyphotesis. Consider a solid body $\Omega \in \mathbb{R}^{n_{dim}}$ with external surface $\delta\Omega \in \mathbb{R}^{n_{dim}-1}$ of outward normal $\mathbf{n}$. In addition, the existence of an interface Γ_i and a discrete internal discontinuity Γ_l is formulated. The position of an arbitrary point is noted by the vector $\mathbf{x}$ in the global Cartesian axis in the bulk, while x_c denotes a material point of Γ_i.

With respect to the surface, there is a decomposition in $\delta\Omega_u$ where the displacement $\mathbf{u}$ is prescribed by Dirichlet-type boundary conditions and $\delta\Omega_t$ where the traction $\mathbf{t}$ is prescribed via Neumann-type conditions (with $\delta\Omega_t \cup \delta\Omega_u = \delta\Omega$ & $\delta\Omega_t \cap \delta\Omega_u = \emptyset$). Also, a body force field per volume $\boldsymbol{f_v}$: $\Omega \in \mathbb{R}^{n_{dim}}$ may be also considered within the solid.

Besides these stated conditions, all of them related to deformation facts, to the same solid, now it will be applied the boundary conditions which are linked to phase field and mass transport.

About phase field boundary conditions, it can be prescribed a Dirichlet condition in ϕ on the crack of the solid. In addition to this, a microtraction f may be denoted in the surface $\delta\Omega_f$.

About hydrogen concentration boundary conditions, the surface might be divided into two parts: $\delta\Omega_q$, when the hydrogen flux $\boldsymbol{J}$ is known and there is a Neumann-type condition; and $\delta\Omega_C$ where the hydrogen concentration C is prescribed.

3.2 Numerical implementation in the bulk

3.2.1 Governing equations

Following Martínez-Pañeda et al. [1], the principle of virtual work in the absence of body forces and in presence of HE reads

$$\underbrace{\int_\Omega \left(\boldsymbol{\sigma} : \nabla\delta\boldsymbol{u} + \omega\delta\phi + \boldsymbol{\zeta}\cdot\nabla\delta\phi - \frac{dC}{dt}\delta\mu + \boldsymbol{J}\cdot\nabla\delta\mu \right) \mathrm{d}\Omega}_{\delta\mathscr{W}_i} = \underbrace{\int_{\delta\Omega} \left(t\cdot\delta u + f\delta\phi + q\delta\mu \right) \mathrm{d}S}_{\delta\mathscr{W}_e} \tag{3.1}$$

where $\delta\mathscr{W}_i$ and $\delta\mathscr{W}_e$ are the internal & external work, respectively and μ stands for the chemical potencial, ω and $\boldsymbol{\zeta}$ are microstress quantities work conjugated to the phase field parameter ϕ and its gradient $\nabla\phi$, respectively.

If the product rule and Gauss'divergence theorem are applied to the internal work $\delta\mathscr{W}_i$, it renders:

$$\delta\mathscr{W}_i = \int_{\delta\Omega}\left(\boldsymbol{\sigma}\boldsymbol{n}\cdot\delta\boldsymbol{u}+\boldsymbol{\zeta}\cdot\boldsymbol{n}\delta\phi+\boldsymbol{J}\cdot\boldsymbol{n}\delta\mu\right)\mathrm{d}S-\int_{\Omega}\left((\nabla\cdot\boldsymbol{\sigma})\cdot\delta\mu+(\nabla\cdot\boldsymbol{\zeta}-\omega)\delta\phi+\left(\nabla\cdot\boldsymbol{J}+\frac{dC}{dt}\right)\delta\mu\right)\mathrm{d}\Omega \tag{3.2}$$

Due to the second integral on the right-hand side of eq. 3.2 having to vanish for arbitrary variations, a set of three equilibrium equations is obtained:

$$\nabla\cdot\boldsymbol{\sigma}=\mathbf{0}\ on\ \Omega \tag{3.3}$$
$$\nabla\cdot\boldsymbol{\zeta}-\omega=0\ on\ \Omega \tag{3.4}$$
$$\frac{dC}{dt}+\nabla\cdot\boldsymbol{J}=0\ on\ \Omega \tag{3.5}$$

In addition to this, as the first integral on the right hand side of eq. 3.2 corresponds to the external work, by accounting for the right side of eq. 3.1, the following boundary conditions related to the surface are obtained:

$$\boldsymbol{t}=\boldsymbol{\sigma}\cdot\boldsymbol{n}\ on\ \delta\Omega_t \tag{3.6}$$
$$f=\boldsymbol{\zeta}\cdot\boldsymbol{n}\ on\ \delta\Omega_f \tag{3.7}$$
$$q=\boldsymbol{J}\cdot\boldsymbol{n}\ on\ \delta\Omega_q \tag{3.8}$$

3.2.2 Energy balance

The first two laws of thermodynamics in a dynamic process of specific internal energy $\mathscr{E}$ and a specific entropy Λ may be read as:

$$\frac{d}{dt}\int_{\Omega}\mathscr{E}\mathrm{d}\Omega=\delta\mathscr{W}_e(\Omega)-\int_{\delta\Omega}\boldsymbol{Q}\cdot\boldsymbol{n}\mathrm{d}S+\int_{\Omega}Q\mathrm{d}\Omega \tag{3.9}$$

$$\frac{d}{dt}\int_{\Omega}\Lambda\mathrm{d}\Omega\geq\int_{\delta\Omega}\frac{\boldsymbol{Q}}{\Theta}\cdot\boldsymbol{n}\mathrm{d}S+\int_{\Omega}\frac{Q}{\Theta}\mathrm{d}\Omega \tag{3.10}$$

where $\delta\mathscr{W}_e$ is the external work; $\boldsymbol{Q}$, the heat flux; Q, the heat absorbtion and Θ, the absolute temperature.

Within a isothermal process (Θ = constant), the thermodynamic laws (eqs. 3.9 & 3.10) might be combined by employing the free energy expression

$$\psi=\mathscr{E}-\Theta\Lambda \tag{3.11}$$

such that:

$$\frac{d}{dt}\int_{\Omega}\psi\mathrm{d}\Omega\leq W_e(\omega) \tag{3.12}$$

which is the Clausius-Duhem inequality or the principle of dissipation [59].

If the external work from eq. 3.1 is substituted into ineq. 3.12, this takes the form

$$\frac{d}{dt}\int_{\Omega}\psi\mathrm{d}\Omega\leq\int_{\delta\Omega_t}\boldsymbol{t}\cdot\dot{\boldsymbol{u}}\mathrm{d}S+\int_{\delta\Omega_f}f\cdot\dot{\phi}\mathrm{d}S+\int_{\delta\Omega_q}q\cdot\dot{\mu}\mathrm{d}S \tag{3.13}$$

At last, if the divergence theorem is employed and eqs. 3.3-3.8 are considered, the local dissipation postulate is reached

$$\boldsymbol{\sigma}:\nabla\dot{\boldsymbol{u}}+\omega\dot{\phi}+\zeta\cdot\nabla\dot{\phi}+\mu\dot{C}+\boldsymbol{J}\cdot\nabla\mu-\dot{\psi}\leq0 \tag{3.14}$$

3.2.3 Constitutive theory

It is constructed in a thermodynamically consistent manner, by ensuring that the dissipation condition (eq. 3.14) is herein satisfied. Accordingly, the free energy ψ is defined as

$$\begin{aligned}\psi(\boldsymbol{\varepsilon},\phi,\nabla\phi,C) = &\underbrace{(1-\phi)^2\psi_0(\boldsymbol{\varepsilon}) - K\bar{V}_H(C-C^0)tr\boldsymbol{\varepsilon}}_{\psi^b} \\ &+\underbrace{\mathscr{G}_C(\theta_H)\left(\frac{1}{2\ell}\psi^2+\frac{\ell}{2}|\nabla\phi|^2\right)}_{\psi^s} \\ &+\underbrace{\mu^0 C + RTN(\theta_L\ln\theta_L+(1-\theta_L)\ln(1-\theta_L))}_{\psi^c}\end{aligned} \tag{3.15}$$

where $\psi_b(\boldsymbol{\varepsilon},\phi,C)$, $\psi_s(\psi,\nabla\psi,C)$ and $\psi_C(C)$ denote the chemo-elastic stored energy in the bulk [60], the crack surface energy and the free chemical energy, respectively; K, the bulk modulus; $\boldsymbol{\varepsilon}$, the strain tensor; C_0, the reference lattice hydrogen concentration; $\bar{V}_H$, the partial molar volume of hydrogen in solid solution; θ_L, the occupancy of lattice sites; N, the number of lattice sites; and μ_0, the reference chemical potential.

Free energy terms disposed in eq. 3.15 are herein represented.

Mechanical deformation

The elastic strain energy density for the intact bulk $\psi_0(\boldsymbol{\varepsilon})$ is given as

$$\psi_0(\boldsymbol{\varepsilon}) = \frac{1}{2}\boldsymbol{\varepsilon}^T : \boldsymbol{C_0} : \boldsymbol{\varepsilon} \tag{3.16}$$

where $\boldsymbol{C_0}$ stands for the linear elastic stiffness matrix.

A linear elastic description in the material response is appropiate to reproduce the brittle behaviour of metals in the presence of hydrogen. Multi-scale plasticity formulations have shown that crack tip stresses are more precise than the ones obtained via conventional theories, such as [61] [62] [63].

Small strains are assumed and therefore, the strain tensor $\boldsymbol{\varepsilon}$ is defined as

$$\boldsymbol{\varepsilon} = \frac{1}{2}[\nabla\boldsymbol{u}^T + \nabla\boldsymbol{u}] \tag{3.17}$$

Hence, Cauchy stress tensor $\boldsymbol{\sigma}$ may be obtained by eq. 3.15 as

$$\boldsymbol{\sigma} = \frac{\partial\psi}{\partial\boldsymbol{\varepsilon}} = g(\psi)(\boldsymbol{C_0} : \boldsymbol{\varepsilon}) - K\bar{V}_H(C-C^0)\boldsymbol{I} \tag{3.18}$$

It can be seen that the second term has a negligible effect in the hydrogen embrittlement phenomena [64]. As it was shown in section 2.2, phase field model reproduces the bond breakage, which leads to loss in stiffness, by the means of the degradation function $g(\phi)$.

Phase field fracture

The expression for the scalar microstress ω, work conjugate to the phase field parameter ϕ, which are easily obtained by deriving from the free chemical energy expression in eq. 3.15, reads

$$\omega = \frac{\partial\psi}{\partial\phi} = -2(1-\phi)\psi_0(\boldsymbol{\varepsilon}) + \mathscr{G}_C(\theta_H)\frac{1}{\ell}\phi \tag{3.19}$$

as well as the one for the vector microstress ζ, work conjugate to the phase field gradient $\nabla\phi$

$$\zeta = \frac{\partial\psi}{\partial\nabla\phi} = +\mathscr{G}_C(\theta_H)\ell\nabla\phi \tag{3.20}$$

If these constitutive relations are inserted in the local balance of eq. 3.4, eq. 2.21 is obtained if the concentration gradient along the small region where $\nabla\phi \neq 0$ is neglected.

First, the fracture phase field is driven by the deformation of the solid through the strain energy density ψ_0. On the other hand, connection between the phase field fracture and hydrogen diffusion is bonded by defining a crack surface energy which depends on hydrogen coverage and that models decohesion enhancement by

H_2. This last coupling is provided via a quantum-mechanical degradation law in a multi-scale fashion (see section 2.3).

Mass transport

The gradient of the chemical potencial $\nabla\mu$ drives the hydrogen transport. The chemical potential may be derived from the free energy (eq. 3.15) by considering the relation between the occupancy and the number of lattice sites, $\theta_L = \frac{C}{N}$.

$$\mu = \frac{\partial \psi}{\partial C} = \mu^0 + RT \ln \frac{\theta_L}{1-\theta_L} - \bar{V}_H \sigma_H + \mathscr{G}'_C(\theta_H)\theta'_H \left(\frac{1}{2\ell}\phi^2 + \frac{\ell}{2}|\nabla\phi|^2 \right) \tag{3.21}$$

Accordingly, hydrogen atoms migrate from regions of high chemical potential to low chemical potential. Coupling with the deformation of the solid is given by the stress-dependent fragment of μ. As it says in eq. 3.21, hydrostatic tensile stresses σ_H increase hydrogen solubility in the lattice (favouring its dilation) with the decreasing in the chemical potencial μ. Furthermore, the last term in eq. 3.21 favours diffusion from cracked regions to intact regions. Nevertheless, appropiate chemical boundary conditions in a propagating crack require deeper analysis.

The constitutive formulation is completed by the expression for the mass flux, which is expressed with a linear Onsager relationship.

$$\boldsymbol{J} = -\frac{DC}{RT}\nabla\mu \tag{3.22}$$

where D stands for the diffusion coefficient.

3.2.4 Numerical formulation & FE discretization

FEM is employed to solve the coupled transport-deformation-phase field problem. Through the explotation of Voigt notation is employed, the nodal values of the displacements, phase field parameter and hydrogen concentration are interpolated as follows

$$\boldsymbol{u} = \boldsymbol{N}\hat{\boldsymbol{d}}, \quad \phi = \boldsymbol{N}\hat{\boldsymbol{\phi}}, \quad C = \boldsymbol{N}\hat{\boldsymbol{C}} \tag{3.23}$$

where $\boldsymbol{N}$ denote the interpolation matrices and $\hat{\boldsymbol{d}}$, $\hat{\boldsymbol{\phi}}$ and $\hat{\boldsymbol{C}}$ the nodal values for displacements, phase field parameter and hydrogen concentration parameters, respectively. Their matrix notation is expressed as

$$\boldsymbol{u} = \sum_{i=1}^{m} N_u \boldsymbol{u}_i, \quad \phi = \sum_{i=1}^{m} N_\phi \phi_i, \quad C = \sum_{i=1}^{m} N_C C_i \tag{3.24}$$

where m stands for the number of nodes and N_i the nodal shape functions.

The corresponding gradient quantities may be discretized as

$$\boldsymbol{\varepsilon} = \sum_{i=1}^{m} \boldsymbol{B}_u \boldsymbol{u_i}, \quad \nabla\phi = \sum_{i=1}^{m} \boldsymbol{B}_\phi \phi_i, \quad \nabla C = \sum_{i=1}^{m} \boldsymbol{B}_C C_i \tag{3.25}$$

where $\boldsymbol{B}_\phi$ & $\boldsymbol{B}_C$ are the vectors with the spatial derivatives of the shape functions of ϕ & C; and $\boldsymbol{B_u}$, the standard strain matrices.

FE discretization of the deformation-phase field fracture problem

Weak form of the deformation problem may be written as

$$\int_\Omega \Big(g(\phi)\boldsymbol{\sigma}_0 : \delta\boldsymbol{\varepsilon} - \boldsymbol{b}\cdot\delta\boldsymbol{u} \Big) \mathrm{d}\Omega - \int_{\Omega_t} (\boldsymbol{t}\cdot\delta\boldsymbol{u}) \mathrm{d}S = 0 \tag{3.26}$$

where $\boldsymbol{\sigma}_0$ stands for the Cauchy stress tensor for the intact bulk. Employing the FE discretization stated at section 3.2.4 and considering that eq. 3.26 must be verified for arbitrary values of $\delta\boldsymbol{u}$, the discrete equation referred to the equilibrium condition may be rewritten as a residual with respect to the displacement field $\boldsymbol{r}_i^{\boldsymbol{u}}$.

$$\boldsymbol{r}_i^{\boldsymbol{u}} = \int_\Omega [(1-\phi)^2 + \kappa](\boldsymbol{B}_i^u)^T \boldsymbol{\sigma}_0 \mathrm{d}\Omega - \int_\Omega \boldsymbol{N}_i^T \boldsymbol{b} \mathrm{d}\Omega - \int_{\delta\Omega_t} N_i^T \boldsymbol{t} \mathrm{d}S \tag{3.27}$$

Similarly to this, the force residual with respect to the phase field fracture is obtained by discretizing eq. 2.20 and considering the contribution for the conjugate microtraction at eq. 3.1,

$$r_i^{\phi} = \int_{\Omega} \left[-2(1-\phi)N_i H + \mathscr{G}_C(\theta_H)\left(\frac{1}{\ell}N_i\phi + \ell \boldsymbol{B}_i^T \nabla\phi\right)\right] \mathrm{d}\Omega - \int_{\delta\Omega_f} N_i^T f \mathrm{d}S \tag{3.28}$$

where H stands for the so-called history variable field, introduced to ensure irreversibility

$$H = \begin{cases} \psi_0(\boldsymbol{\varepsilon}) & \text{if } \psi_0(\boldsymbol{\varepsilon}) \geq H_t \\ H_t & \text{otherwise} \end{cases} \tag{3.29}$$

where H_t denotes the pre-calculated energy at time increment t. This is done in order to satisfy the Kuhn–Tucker conditions.

Components of the corresponding stiffness matrices are obtained by differenciating the residuals with respect to the incremental nodal variables

$$\boldsymbol{K}_{ij}^{uu} = \frac{\partial \boldsymbol{r}_i^u}{\partial \boldsymbol{u}_j} = \int_{\Omega} [(1-\phi)^2 + \kappa](\boldsymbol{B}_i^u)^T \boldsymbol{C}_0 \boldsymbol{B}_j^u \mathrm{d}\Omega \tag{3.30}$$

$$\boldsymbol{K}_{ij}^{\phi\phi} = \frac{\partial r_i^{\phi}}{\partial \phi_j} = \int_{\Omega} \left[\left(2H + \frac{\mathscr{G}_C(\theta_H)}{\ell}\right) N_i N_j + \mathscr{G}_C(\theta_H)\ell \boldsymbol{B}_i^T \boldsymbol{B}_j \right] d\Omega \tag{3.31}$$

FE discretization of the hydrogen transport problem

If the constitutive equation for the chemical potential μ (eq. 3.21) is substituted into the expression for the mass flux $\boldsymbol{J}$ (eq. 3.22), it is obtained

$$\boldsymbol{J} = -\frac{DC}{1-\theta_L}\left(\frac{\nabla C}{C} - \frac{\nabla N}{N}\right) + \frac{D}{RT} C \bar{V}_H \nabla\sigma_H \tag{3.32}$$

whether low occupancy ($\theta_L << 1$) and constant interstitial sites concentration ($\nabla N = 0$) are supposed, the equation renders

$$\boldsymbol{J} = -D\nabla C + \frac{D}{RT} C \bar{V}_H \nabla\sigma_H \tag{3.33}$$

Substuting in eq. 3.1, the hydrogen transport expression becomes:

$$\int_{\Omega} \left[\delta C \left(\frac{1}{D}\frac{dC}{dt}\right) + \nabla\delta C \nabla C - \nabla\delta C \right] \left(\frac{\bar{V}_H C}{RT}\nabla\sigma_H\right) \mathrm{d}\Omega = -\frac{1}{D}\int_{\delta\Omega_q} \delta C q \mathrm{d}S \tag{3.34}$$

The residual with respect to the hydrogen concentration r_i^C is obtained by discretizing eq. 3.34, taking into account that δC is an arbitrary virtual variation of the hydrogen concentration.

$$r_i^C = \int_{\Omega} \left[N_i^T \left(\frac{1}{D}\frac{dC}{dt}\right) + \boldsymbol{B}_i^T \nabla C - \boldsymbol{B}_i^T \left(\frac{\bar{V}_H C}{RT}\nabla\sigma_H\right)\right] \mathrm{d}\Omega + \frac{1}{D}\int_{\delta\Omega_q} N_i^T q \mathrm{d}S \tag{3.35}$$

from which a diffusivity matrix is herein denoted

$$\boldsymbol{K}_{ij}^{CC} = \int_{\Omega} \left(\boldsymbol{B}_i^T \boldsymbol{B}_j - \boldsymbol{B}_i^T \frac{\bar{V}_H}{RT} \nabla\sigma_H N_j \right) \mathrm{d}\Omega \tag{3.36}$$

Note that in the eq. 3.36 that $\boldsymbol{K}_{ij}^{CC}$ is affected by the gradient of the hydrostatic stress, $\nabla\sigma_H$, which is computed at the integration points from the nodal displacements, extrapolated to the nodes by the employment of the shape functions and consequently, multiplied by $\boldsymbol{B}$. Stemming from the previous formulation, 2D 8-node quadrilateral FE with C_0 continuity are herein employed for the bulk region [1].

On the other hand, the concentration capacity matrix $\boldsymbol{M}_{ij}$ may be identified

$$\boldsymbol{M}_{ij} = \int_{\Omega} N_i^T \frac{1}{D} N_j \mathrm{d}\Omega \tag{3.37}$$

and a diffusion flux factor $\boldsymbol{F}_i$

$$\boldsymbol{F}_i = -\frac{1}{D}\int_{\delta\Omega_q} N_i^T q \mathrm{d}\delta\Omega_q \tag{3.38}$$

Consequently, the global equation for hydrogen renders

$$\boldsymbol{K}^{CC}\boldsymbol{C} + \boldsymbol{M}\dot{\boldsymbol{C}} = \boldsymbol{F} \tag{3.39}$$

3.2.5 Coupled scheme

The deformation, phase field and hydrogen transport parameters are weekly coupled. Mechanical deformation is related to hydrogen through the stress field, by the pressure dependence of the bulk chemical potencial μ. Next, diffusion of hydrogen affects fracture resistance via hydrogen coverage θ_H, reducing the critical energy release rate $\mathscr{G}_C$. Lastly, phase field degrades the strain energy density ψ of the solid.

The following linear finite element system is herein proposed

$$\begin{bmatrix} \boldsymbol{K}^{uu} & 0 & 0 \\ 0 & \boldsymbol{K}^{\phi\phi} & 0 \\ 0 & 0 & \boldsymbol{K}^{CC} \end{bmatrix} \begin{bmatrix} \boldsymbol{u} \\ \boldsymbol{\phi} \\ \boldsymbol{C} \end{bmatrix} + \begin{bmatrix} 0 & 0 & 0 \\ 0 & 0 & 0 \\ 0 & 0 & \boldsymbol{M} \end{bmatrix} \begin{bmatrix} \dot{\boldsymbol{u}} \\ \dot{\boldsymbol{\phi}} \\ \dot{\boldsymbol{C}} \end{bmatrix} = \begin{bmatrix} \boldsymbol{r}^{\boldsymbol{u}} \\ \boldsymbol{r}^{\boldsymbol{\phi}} \\ \boldsymbol{r}^{\boldsymbol{C}} \end{bmatrix} \tag{3.40}$$

A time parametrization and a incremental-iterative scheme are employed in conjunction with the Newton-Raphson method. Deformation and phase field coupling is solved with the staggered solution scheme proposed by Miehe et al. [42].

3.3 Numerical implementation in the interface

The numerical strategy followed in order to solve the quasi-static evolution problems for brittle fracture in the cohesive fracture along the interfaces goes along with the formulation proposed in section 2.3, developed by Paggi and Reinoso [2].

First of all, nodal values of displacements and phase field parameter are interpolated the same manner as the bulk (see section. 3.2.4)

Framework is started with the discretization of eq. 2.34 for each interface finite element Γ_i^{el} ($\Gamma_i \sim \cup\Gamma_i^{el}$)

$$\delta\tilde{\Pi}^{el}_{\Gamma_i}(\boldsymbol{u_i},\delta\boldsymbol{u_i},\bar{\phi},\delta\bar{\phi}) = \int_{\Gamma_i^{el}} \left(\frac{\partial\mathscr{G}^i(\boldsymbol{u_i},\bar{\phi})}{\partial\boldsymbol{u_i}}\delta\boldsymbol{u_i} + \frac{\partial\mathscr{G}^i(\boldsymbol{u_i},\bar{\phi})}{\partial\phi_i}\delta\bar{\phi} \right) \mathrm{d}\Gamma \tag{3.41}$$

where $\mathscr{G}^i = \mathscr{G}^i_I + \mathscr{G}^i_{II}$.

The displacement gap vector $\boldsymbol{g}$ at any point inside the elements of the interface Γ_i^{el} stands for the result of the difference between the displacements of the opposing points at both interface sides, which is obtained with the interpolation of the nodal displacements $\boldsymbol{u_i}$ multiplied by the matrix operator $\boldsymbol{L}$ and the collector matrix for the Lagrangian shape functions $\boldsymbol{N_u}$ of the displacement field.

$$\boldsymbol{g} = \boldsymbol{N}_u\boldsymbol{L}\boldsymbol{u_i} = \boldsymbol{B}_u\boldsymbol{u_i} \tag{3.42}$$

where $\boldsymbol{B}_u$ denotes the compatibility operator.

In order to apply the CZM relation, expressed in a local reference system defined by the normal and tangential directions at the interface [67] [68], the global gap vector $\boldsymbol{g}$ is multiplied by the rotation matrix R to obtain the local gap $\boldsymbol{g}_{loc}$.

$$\boldsymbol{g}_{loc} = \boldsymbol{R}\boldsymbol{g} = \boldsymbol{R}\boldsymbol{B}_u\boldsymbol{u_i} \tag{3.43}$$

Following the same pattern, the average phase field variable ϕ is computed across the interface Γ_{el}.

$$\phi = \boldsymbol{N}_\phi\boldsymbol{M}_\phi\bar{\phi} = \boldsymbol{B}_\phi\bar{\phi} \tag{3.44}$$

where $\boldsymbol{M}_\phi$ stands for an average operator and $\boldsymbol{B}_\phi$, the compatibility operator for the phase field parameter ϕ. Further research about the operators for the current cohesive formulation for two-dimensional and three-dimensional applications are found in [69] [68].

Then, the discretized weak form renders

$$\begin{aligned}\delta\tilde{\Pi}^{el}_{\Gamma_i}(\boldsymbol{u_i},\delta\boldsymbol{u_i},\bar{\phi},\delta\bar{\phi}) &= \delta\boldsymbol{u_i^T}\int_{\Gamma_i^{el}}\left(\frac{\partial\mathscr{G}^i(\boldsymbol{u_i},\bar{\phi})}{\partial\boldsymbol{u_i}}\right)^T\mathrm{d}\Gamma+\delta\bar{\phi}^T\int_{\Gamma_i^{el}}\left(\frac{\partial\mathscr{G}^i(\boldsymbol{u_i},\bar{\phi})}{\partial\bar{\phi}}\right)^T\mathrm{d}\Gamma \\ &= \delta\boldsymbol{u_i^T}\int_{\Gamma_i^{el}}\boldsymbol{B}^T\boldsymbol{R}^T\left(\frac{\partial\mathscr{G}^i(\boldsymbol{u_i},\bar{\phi})}{\partial\boldsymbol{g}_{loc}}\right)^T\mathrm{d}\Gamma+\delta\bar{\phi}^T\int_{\Gamma_i^{el}}\boldsymbol{B}^T\left(\frac{\partial\mathscr{G}^i(\boldsymbol{u_i},\bar{\phi})}{\partial\phi}\right)^T\mathrm{d}\Gamma\end{aligned} \tag{3.45}$$

which leads to the residual vectors for deformation & phase field

$$\boldsymbol{r^u} = \int_{\Gamma_i^{el}}\boldsymbol{B}^T\boldsymbol{R}^T\left(\frac{\partial\mathscr{G}^i(\boldsymbol{u_i},\bar{\phi})}{\partial\boldsymbol{g}_{loc}}\right)^T\mathrm{d}\Gamma \tag{3.46}$$

$$\boldsymbol{r^\phi} = \int_{\Gamma_i^{el}}\boldsymbol{B}_\phi^T\left(\frac{\partial\mathscr{G}^i(\boldsymbol{u_i},\bar{\phi})}{\partial\phi}\right)^T\mathrm{d}\Gamma \tag{3.47}$$

Through the differentiation of the residual vectors, the stiffness matrices of the proposed interface finite element for the displacements $\boldsymbol{u}$ and the phase field parameter ϕ are derived:

$$\boldsymbol{K^{uu}} = \frac{\partial r^u}{\partial\boldsymbol{u}} = \int_{\Gamma_i^{el}}\boldsymbol{B}^T\boldsymbol{R}^T\mathbb{C}_{\boldsymbol{uu}}\boldsymbol{R}\boldsymbol{B}\mathrm{d}\Gamma \tag{3.48}$$

$$\boldsymbol{K^{u\phi}} = \frac{\partial r^u}{\partial\phi} = \int_{\Gamma_i^{el}}\boldsymbol{B}^T\boldsymbol{R}^T\mathbb{C}_{\boldsymbol{u\phi}}\boldsymbol{B}_\phi\mathrm{d}\Gamma \tag{3.49}$$

$$\boldsymbol{K^{\phi u}} = \frac{\partial r^\phi}{\partial\boldsymbol{u}} = \int_{\Gamma_i^{el}}\boldsymbol{B}_\phi^T\mathbb{C}_{\phi\boldsymbol{u}}\boldsymbol{R}\boldsymbol{B}\mathrm{d}\Gamma \tag{3.50}$$

$$\boldsymbol{K^{\phi\phi}} = \frac{\partial r^\phi}{\partial\phi} = \int_{\Gamma_i^{el}}\boldsymbol{B}_\phi^T\mathbb{C}_{\phi\phi}\boldsymbol{B}_\phi\mathrm{d}\Gamma \tag{3.51}$$

where the tangent constitutive operators of the interface $\mathbb{C}$ have the following form for the present framework:

$$\mathbb{C}^{\boldsymbol{uu}} = \begin{bmatrix}\hat{\alpha}k_n & 0\\ 0 & \hat{\beta}k_t\end{bmatrix} \tag{3.52}$$

$$\mathbb{C}^{\boldsymbol{u\phi}} = \begin{bmatrix}g_nk_n\frac{\partial\hat{\alpha}}{\partial\phi} & g_tk_t\frac{\partial\hat{\beta}}{\partial\phi}\end{bmatrix} \tag{3.53}$$

$$\mathbb{C}^{\boldsymbol{\phi u}} = \begin{bmatrix}g_nk_n\frac{\partial\hat{\alpha}}{\partial\phi}\\ g_tk_t\frac{\partial\hat{\beta}}{\partial\phi}\end{bmatrix} \tag{3.54}$$

$$\mathbb{C}^{\phi\phi} = \frac{1}{2}g_n^2k_n\frac{\partial^2\hat{\alpha}}{\partial\phi^2}+\frac{1}{2}g_t^2k_t\frac{\partial^2\hat{\beta}}{\partial\phi^2} \tag{3.55}$$

and the terms $\hat{\alpha}$ and $\hat{\beta}$ read:

$$\hat{\alpha} = \frac{g_{nc,0}^2}{[(1-\phi)g_{nc,0}+\phi g_{nc,1}]^2} \tag{3.56}$$

$$\hat{\beta} = \frac{g_{tc,0}^2}{[(1-\phi)g_{tc,0}+\phi g_{tc,1}]^2} \tag{3.57}$$

The coupled system of equations for displacement and phase field parameters takes the form

$$\begin{bmatrix}\boldsymbol{K_{uu}} & \boldsymbol{K_{u\phi}}\\ \boldsymbol{K_{\phi u}} & \boldsymbol{K_{\phi\phi}}\end{bmatrix}\begin{bmatrix}\delta\boldsymbol{u}\\ \delta\phi\end{bmatrix} = \begin{bmatrix}\boldsymbol{r^u_{int}}\\ \boldsymbol{r^\phi_{int}}\end{bmatrix} \tag{3.58}$$

Standard low-order finite elements are used for the spatial discretization, where a fully monolithic coupled solution scheme for the displacement and the phase field nodal variables is considered. The current modeling framework herein presented is focused on 2D applications, although its extension to 3D cases is straightforward.

3.4 Implementation tasks

In this section, the amount of tasks dedicated to this work will be explained, in order to state what has been done by the student of this document:

First of all, he has thoroughly understood both bulk & interface frameworks previously developed. This aspect has included the further reading of both articles, their examples and the results obtained from them. After this, he has interpreted how the codes for both models work; in fact, it has simulated an example provided by the authors of them, which also has allowed him to know how to obtain the output for such instances.

Next, he has discussed how to incorporate the hydrogen concentration to the interface model, a novelty for it which has not been included before. Therefore, it has simulated numerically (employing mathematical software such as *MATLAB*) various proposed models of interface degradation by the hydrogen coverage θ_H until eq. 2.43 has been reached.

Thereupon, he has been focused on the main task of this project: the coupling of both models in a single solid. Accordingly, he has been working with their directors to develop a code which includes both models in the specimen, a task which has been done, as it can be seen by the case studies which will be explained afterwards.

Lastly, but not less important, he has been searching for examples to apply this novel framework, which, in addition to this, may serve as future applications. This will be detailed in chapter 5.

4 Case studies

A number of case studies of particular interest are analyzed in order to test the formulation presented in this chapter.

The problem of a two-grain (with a grain boundary) cracked plate subjected to tension is herein analyzed. Firstly, in order to verify the implementation of the code of Paneda [1], previously developed in section 3.2, it is modelled this benchmark problem with only using his code, subsequently assessing the role of hydrogen. Consequently, same probe is studied, but this time with the coupling of both bulk & interface models, being this last one previously explained in section 3.3, in order to show the capabilities of the modeling framework presented.

4.1 General case

This problem possess a horizontal crack, placed at the middle point of the left side of the left grain, in a hydrogen environment is herein presented. The geometry as well as the boundary conditions are illustrated in fig. 4.1, with the values measured in *mm*.

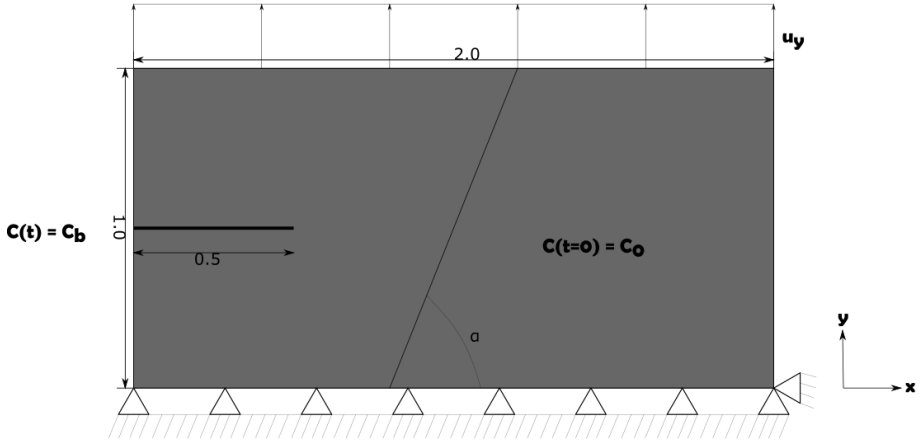

Figure 4.1 Graphic image of the geometry and configuration of the studied cracked plate.

As depicted in 4.1, the bottom edge is fixed only in Y direction (except the right corner, which is also fixed in X direction), while a prescribed vertical displacement is applied on the top edge of $u_y = 0.01\ mm$. Steel properties are applied to the solid, as Young's modulus is $E = 210000\ MPa$ and Poisson's ratio $\nu = 0.3$.

About the hydrogen concentration, an initial condition of uniform hydrogen distribution through the specimen is defined $C(t=0) = C_0$, like is commonly done in laboratory experiments. In addition to this, while loading, it is assumed that the outer surfaces of the specimen are in contact with the electrochemical solution. Therefore, a constant hydrogen concentration at the boundary is imposed, of equal magnitude to the initially prescribed one, $C_b = C_0$.

A long testing pseudo-time (about $t_f = 1 \cdot 10^7\ s$) is defined in order to allow hydrogen to redistribute in the fracture process zone. An iron-based material is assumed and subsequently, a hydrogen damage coefficient of $\chi = 0.89$ is adopted. Also, a partial molar volume of $\bar{V}_H = 2000\ mm^3/mol$ and a diffusion coefficient of $D = 0.0127\ mm^2/s$ are defined. As the code units of N, mol and mm are adopted; thus the gas constant is defined by $R = 8314\ \frac{N \cdot mm}{mol \cdot K}$.

4.2 Ideal grain boundary cases

4.2.1 Overview

Due to the fact of only using Martínez-Pañeda framework for bulk solid in these first series of cases, grain boundaries will be modelled as ideal, therefore, they will not represent a barrier for crack propagation. Their mechanical properties will be the same as the left grain.

Both grains are meshed in order to provide an accurate example, being specially refined in the potential crack propagation path, due to phase field technique requiring this aspect to resolve the fracture process zone (as well as the rest of discrete techniques). A total of 15396 8-node quadrilateral plane strain elements of reduced integration ($CPE8R$) are employed, with the characteristic element length along the crack propagation path being equal to $h = 0.005\ mm$, 10 times shorter than the length scale $\ell = 0.05\ mm$. Views of the mesh

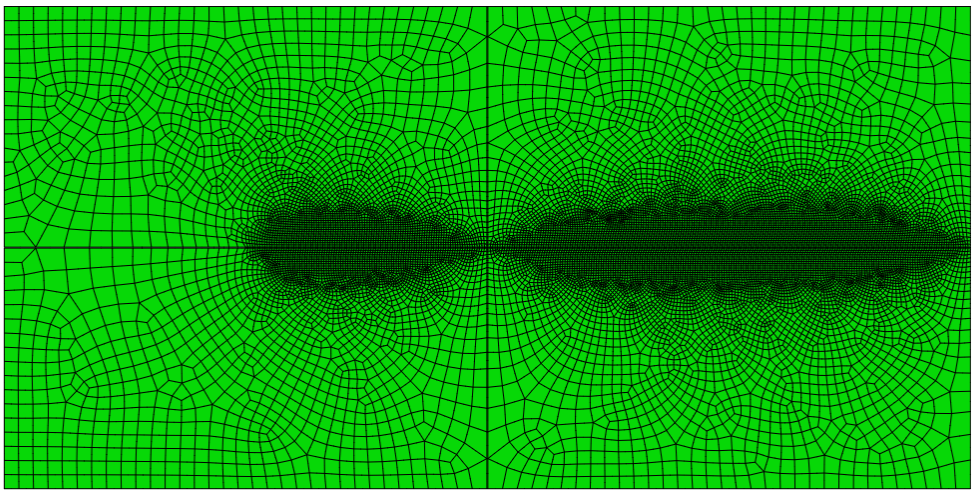

Figure 4.2 Employed mesh for cracked plate structure cases employing only the bulk model.

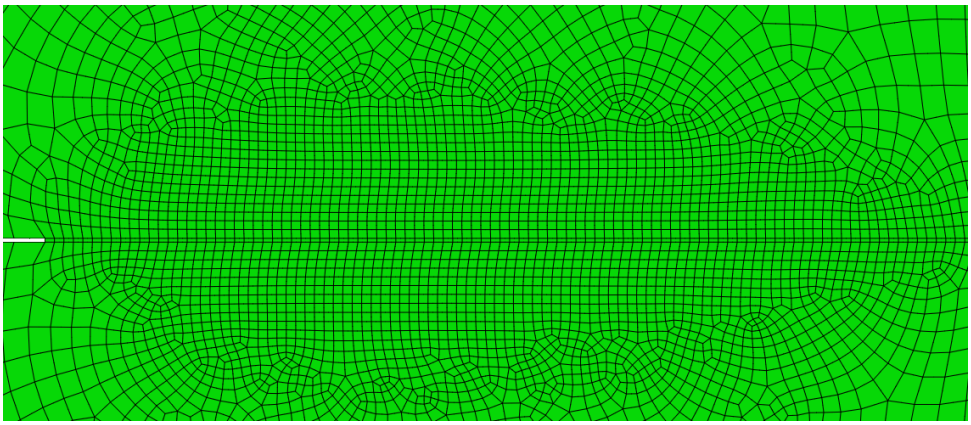

Figure 4.3 Employed mesh for the nearby crack propagation zone in the left grain in the cracked plate.

for all the solid and for the nearby crack propagation zone in the left grain (same is done in all right grain) are displayed at fig. 4.2 & 4.3.

In order to verify the successful implementation of this code for this instance, here it is shown a pair of representative results: in fig. 4.4, it is represented the hydrogen concentration isocontorn along the fracture process zone and in fig. 4.5, crack propagation contours at different load stages. They show a notable match with the ones obtained by Pañeda in [1].

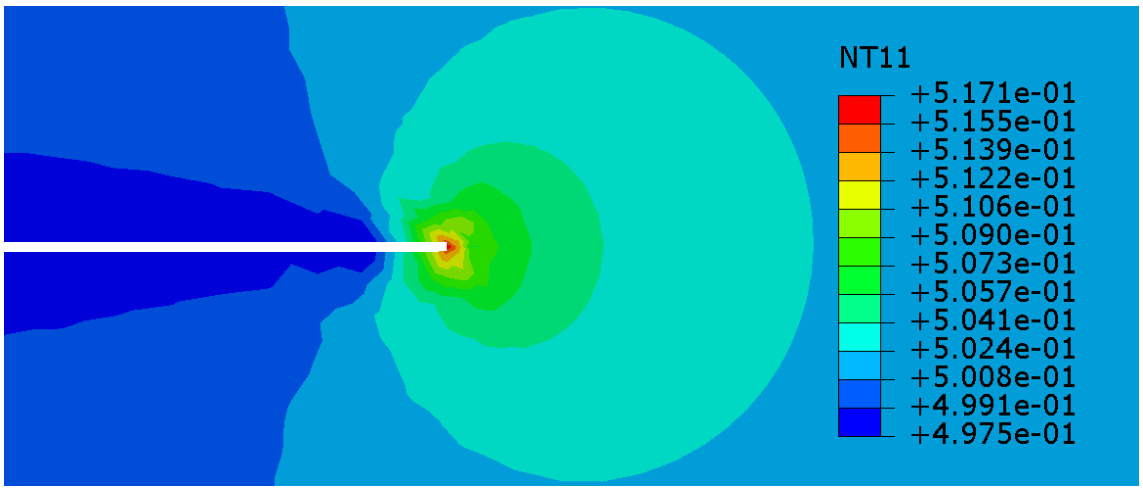

Figure 4.4 Hydrogen concentration in wt ppm in the fracture process zone at the start of crack propagation. Initial concentration of hydrogen for this case is $C_0 = 0.5\ wt\ ppm$..

As it can may be seen in fig. 4.4, hydrogen concentration is accumulated in the fracture process zone around the notch, where hydrostatic stresses are larger.

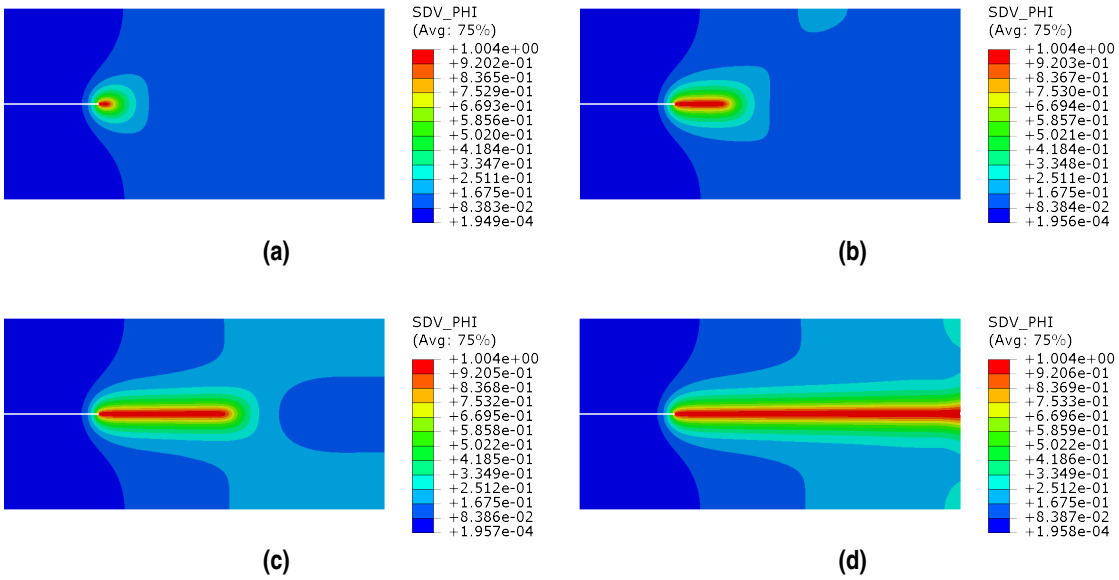

Figure 4.5 Phase field variable map: fracture patterns at different load levels. Initial concentration of hydrogen for this case is $C_0 = 0.5\ wt\ ppm$ in the first grain and $C_0 = 0.1\ wt\ ppm$ in the second one.

In fig. 4.5, phase field parameter ϕ is represented along the solid, where blue and red colors are associated to fully intact and broken state of the material, respectively. In addition to this, it is viewed that the response is not completely symmetric, due to the lower bound being fixed clamped. Also, the crack is rather diffuse, something expected, according to the choice of ℓ.

In the following sections, a parametrical study will be carried out by studying force-displacement curves for various cases of mismatches among both grains in the properties of: 1. boundary hydrogen concentration

C_b, 2. critical energy release rate for both grains $\mathscr{G}_C^b$.

In addition to this, the variation in the inclination angle for the grain boundary α will also be analyzed within this work.

4.2.2 Cases with mismatch in the initial hydrogen concentration

In this first series of cases, the mismatch among both grains in the initial surfacing hydrogen concentration is studied. For the left grain, in every case, an initial surfacing concentration $C_{b,left}$ of 0.5 wt ppm is fixed. On the other hand, for the right grain, four different environments are considered which range from 5 wt ppm to testing in air (fig. 4.6). Furthermore, a vertical grain boundary ($\alpha = 0^\circ$) is added, a critical energy release rate of $G_C^b = 2.7\ MPa \cdot mm$ is set for every grain and the initial hydrogen distribution throughout the specimen is fixed in $C_0 = 0.5\ wt\ ppm$.

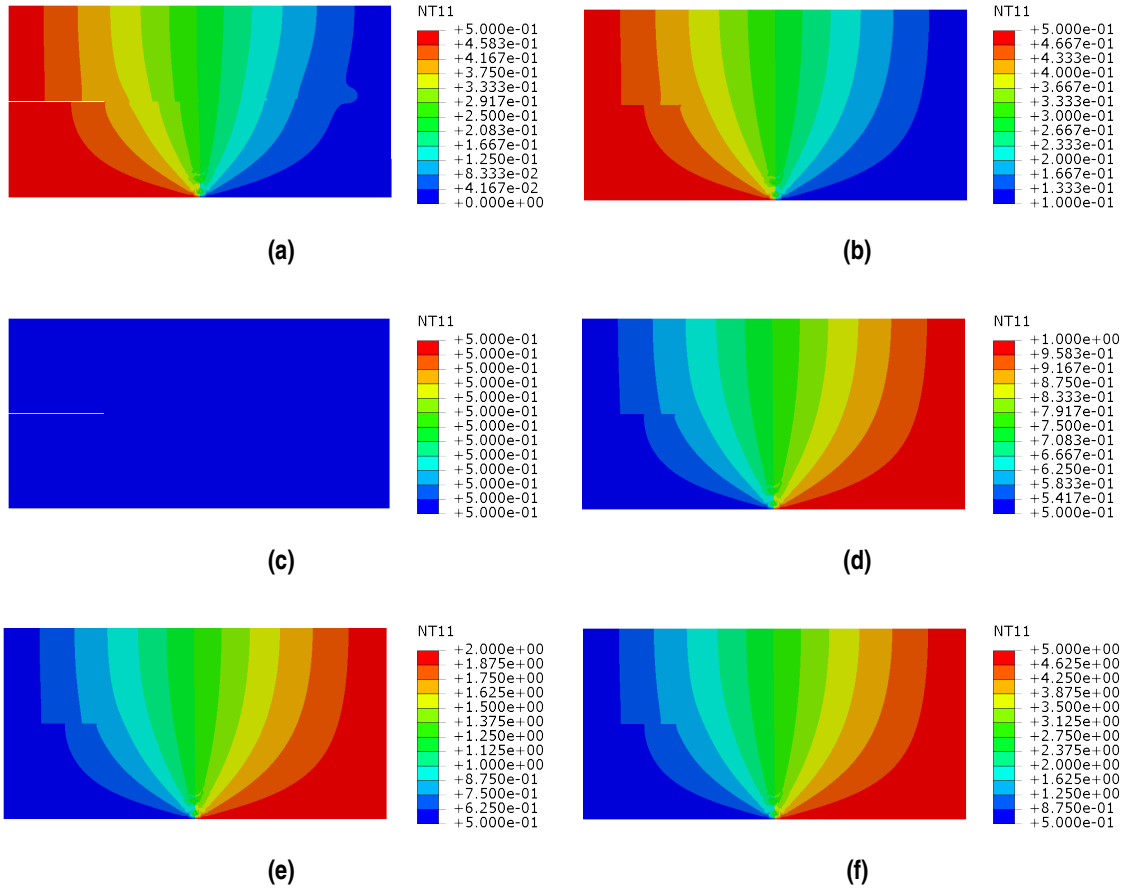

Figure 4.6 Initial hydrogen concentration C_0 isocontorn for every case herein analyzed. From lowest to highest, a) test in air, b) 0.1 wt ppm, c) 0.5 wt ppm, d) 1 wt ppm, e) 2 wt ppm and f) 5 wt ppm for the right grain. For the left grain, $C_{b,left} = 0.5\ wt\ ppm$ is fixed.

In fig. 4.7, the load-displacement graph as a function of the hydrogen concentration for the four environments is shown. As observed in this image, the damage involves an important drop in the load-displacement evolution, associated with the unstable propagation of the crack across the specimen. It follows that the computations proceed without convergence problems up until the load has almost fully dropped. Therefore, the modelling of unstable crack propagation is achieved.

Analyzing the obtained results, it may be seen that by reducing the hydrogen concentration in the right grain, the system can withstand higher load levels, and therefore, more displacement. In table 4.1, maximum forces are displayed, as well as their respective displacements.

Table 4.1 $F_{máx}$ obtained for the cases with variable initial hydrogen concentration $C_{b,right}$ in the right grain.

$C_{b,right}$ $(wt\ ppm)$	$F_{máx}$ (N)	u_y $(10^3\ mm)$
0 (Air)	946.66	3.10
0.1	912.01	3.05
0.5	826.37	2.95
1	768.15	2.85
2	708.87	2.65
5	643.62	2.45

Studying the results summarised in table 4.1, a maximum improvement of 32 % in the $F_{máx}$ (from the extreme case of 5 wt ppm) can be reached by simply removing the hydrogen concentration in the environment of the right grain, an aspect which is remarkable for the fracture toughness of the system, taking into account that the left grain mantains its initial hydrogen concentration value of 0.5 wt ppm (apart from being the one with the notch).

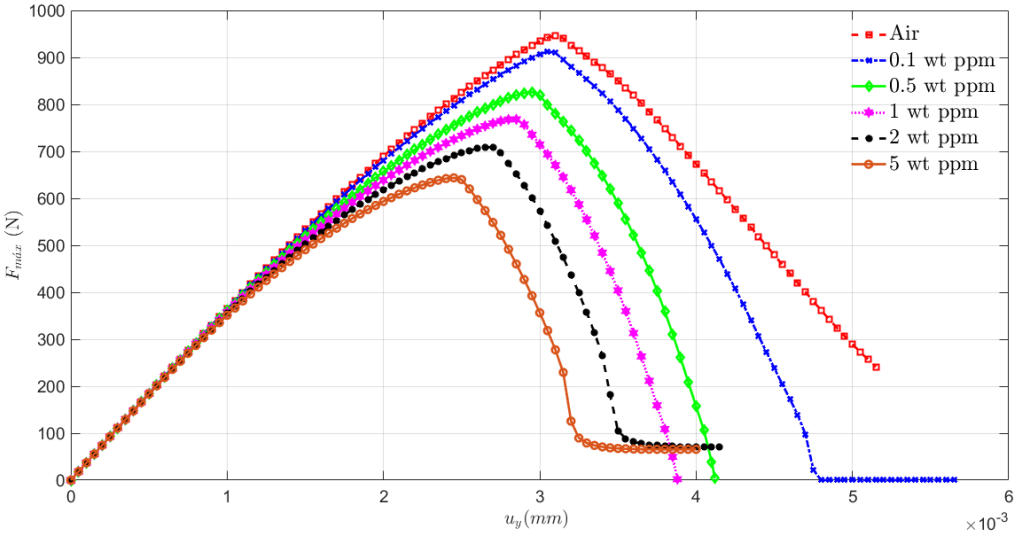

Figure 4.7 Load-displacement curve obtained for the different cases of initial right-grain hydrogen concentration $C_{0,right}$.

4.2.3 Cases with mismatch in the critical energy release rate

Now, similarly to the previous assessment in the prerespect to vious section with respect to C_0, the mismatch among both grains in the critical energy release rate G_C^b is studied. For the left grain, in every case, a value of $G_{C,left}^b = 2.7\ MPa \cdot mm$ of is fixed. On the other hand, for the right grain, five different cases where the $G_{C,right}^b$ varies up from 70 % to 200 % the value of $G_{C,left}^b$ are studied. Also, a vertical grain boundary ($\alpha = 0^\circ$) is supposed and a initial concentration of hydrogen of $C_0 = C_b = 0.5\ wt\ ppm$ is set for all the specimen.

In table 4.2, maximum forces for every different case are displayed, as well as their displacements in that moment. Again, there are slight differences in the peak values for every probe, and it follows that of course, by increasing the critical energy release rate in the right grain, the solid shows a higher maximum force.

In fig. 4.8, the load-deflection curve as a function of the misatch in the critical energy release rate for every single case is herein shown. The same may be said about this picture as the fig. 4.7: all the analysis follow precisely the modelling of unstable crack propagation.

Table 4.2 $F_{máx}$ obtained for the cases with variable critical energy release rate $G^b_{C,right}$ in the right grain..

$G^b_{C,right}$ $(MPa \cdot mm)$	$F_{máx}$ (N)	u_y $(10^3\ mm)$
1.89 (70 % $G^b_{C,left}$)	775.52	2.90
2.16 (80 % $G^b_{C,left}$)	795.69	2.95
2.70 (100 % $G^b_{C,left}$)	826.37	2.95
2.97 (110 % $G^b_{C,left}$)	838.28	2.95
3.51 (130 % $G^b_{C,left}$)	857.51	2.95
4.05 (150 % $G^b_{C,left}$)	872.35	2.95
5.40 (200 % $G^b_{C,left}$)	897.98	2.95

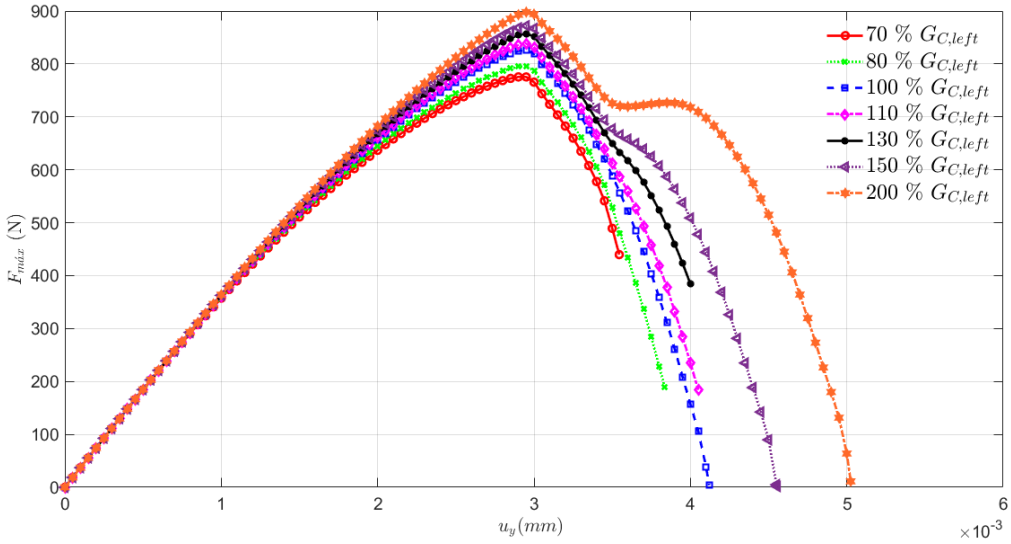

Figure 4.8 Load-displacement curves obtained for the different cases of critical energy release rate in the right grain $G^b_{C,right}$.

Again, if the displayed results in table 4.2 are analyzed, it follows that a maximum improvement of 14 % in the $F_{máx}$ can be achieved by the increasing the value of $G^b_{C,right}$ from 70 %$G^b_{C,left}$ to 200 %$G^b_{C,left}$. Similarly to C_0, this aspect may represent a parameter of consideration for the fracture toughness of the system.

4.2.4 Cases with inclination in the grain boundary

First of all, before attempting any further analysis for this following series of cases, the mesh for the right grain has been refined due to possible deflections of the crack caused. Images of this new mesh are presented in figs. 4.9 & 4.10. Now, a total of $\sim$ 18500 $CPE8R$ elements are employed.

After these slight modifications into the model, the same pattern, that has been employed in the previous examples, is also used here. The slope in the grain boundary is analyzed taking into consideration the restriction caused by the possible distortions in the grain boundary. Here, it has been modelled this parameter up to a value of $\alpha = 30°$ (see fig. 4.10). Moreover, a value for the critical energy release rate of $G^b_C = 2.7\ MPa \cdot mm$ and a initial concentration of hydrogen of $C_0 = C_b = 0.5\ wt\ ppm$ are fixed for the probe.

Load-deflection curve as a function of the degree of the inclination of the grain boundary is shown in fig. 4.9; Analysing the figure, it is seen that all the different examples precisely model the propagation of unstable crack up until the dropping in the load, when the solid collapses, showing no convergence problems in their trayectory.

Maximum forces for every different case and their respective displacements in that moment are displayed in table 4.3. If the trayectory for every case and the peaks in tab. 4.3 are studied, it is extracted that when inclination is introduced ($\alpha > 0$), the maximum force (and, therefore, fracture toughness) barely gets modificated with this addition.

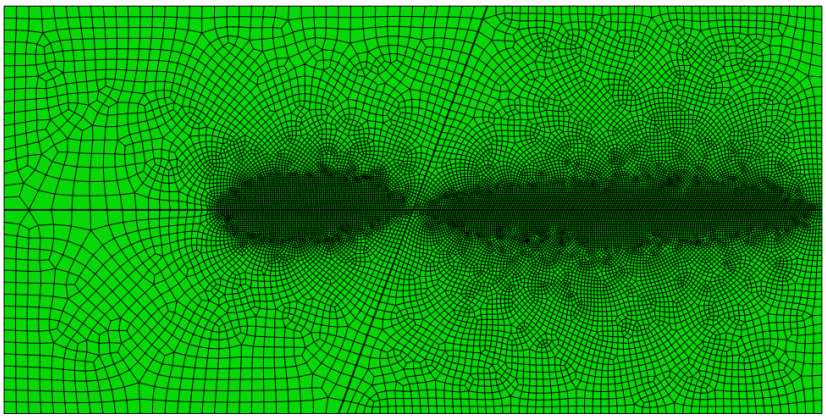

Figure 4.9 Employed mesh for all the cracked plate structure cases with grain boundary inclination. This example corresponds to $\alpha = 20°$.

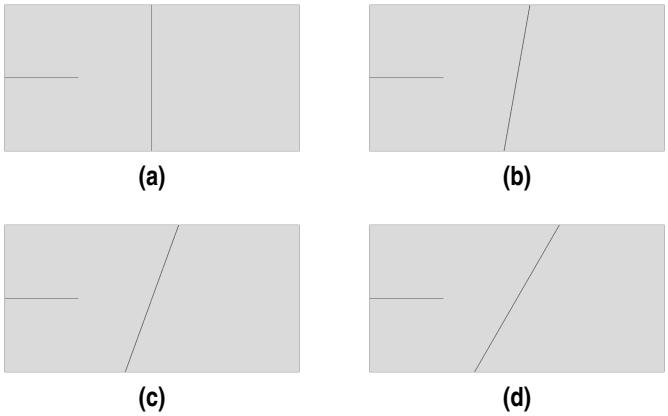

Figure 4.10 Cracked plate structure cases analyzed with variation in the grain boundary inclination. From lowest to highest slope: a) $0°$ (vertical), b) $10°$, c) $20°$ and d) $30°$.

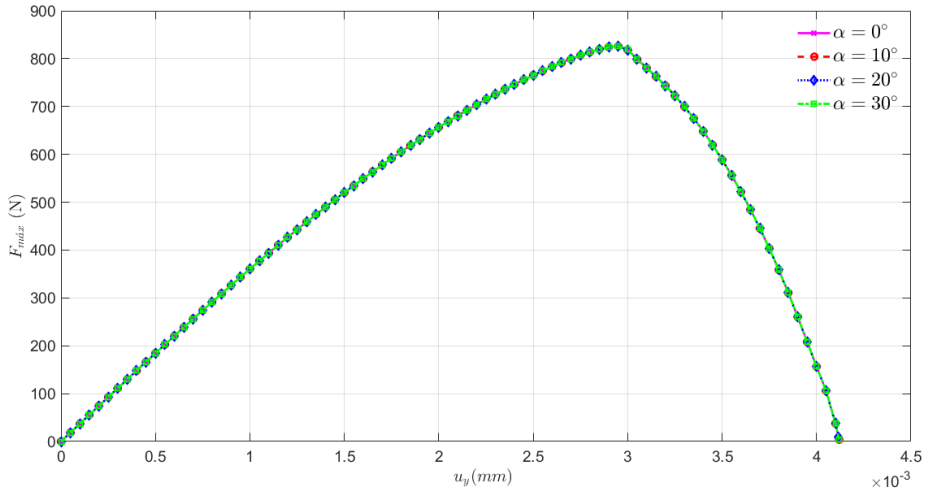

Figure 4.11 Load-displacement curve obtained for the different cases of angle slope α in the grain boundary.

Table 4.3 $F_{máx}$ obtained for the cases with variable inclination degree α in the grain boundary.

α (°)	$F_{máx}$ (N)	u_y $(10^3\ mm)$
0	838.28	2.95
10	826.10	2.95
20	826.14	2.95
30	826.18	2.95

Proof of it is obtained if the crack trayectory is consequently reviewed: it is seen that there is no deflection when it has passed through the grain boundary (fig. 4.12) (something coherent with the implemented model, due to the fixed condition of perfect grain boundary). Because of this, when introducing the cohesive framework for the grain boundary, it is expected to see different results.

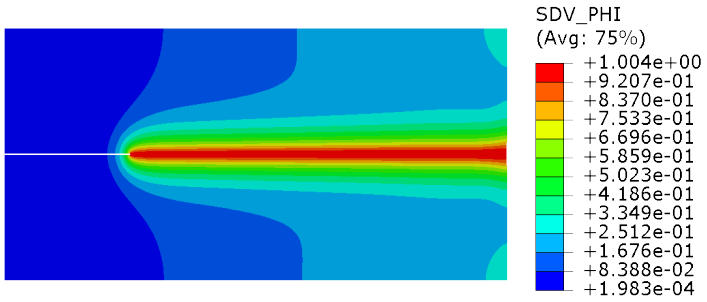

Figure 4.12 Phase field variable map: crack propagation for the example with $\alpha = 30°$, where red and blue symbolize the fully broken and intact states, respectively.

4.2.5 Mixed cases

For this last series of cases from the first example, the combination of the grain boundary inclination α and the mismatch in the critical energy release rate G_C^b or in the initial surfacing hydrogen concentration $C_{b,0}$ will be studied. Then, an inclination degree of $\alpha = 20°$ will be fixed for these numerical studies.

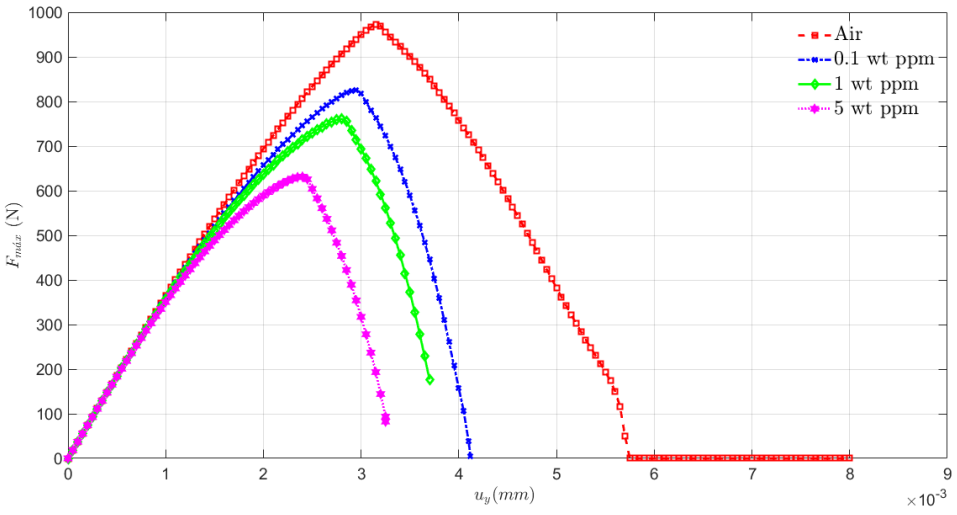

Figure 4.13 Load-displacement curve obtained for the different cases of initial right-grain hydrogen concentration $C_{b,right}$ with inclined grain boundary of $\alpha = 20°$.

First of all, the variation of $C_{b,right}$ is studied. In fig. 4.13, the load-deflection curve for 4 cases ranging from air (0 wt ppm) to 5 wt ppm in $C_{b,right}$ is represented. Like in the vertical grain boundary instances,

$C_{b,left}$ is fixed to 0.5 wt ppm. Moreover, a value for the critical energy release rate of $G_C^b = 2.7\ MPa \cdot mm$ is predefined and the initial hydrogen distribution through the specimen is fixed in $C_0 = 0.5\ wt\ ppm$.

Deepening in the obtained results, the tab. 4.3 shows the peaks of the reaction forces from the fixed surface, as well as their respective displacements in that moment. It follows that, like in the $\alpha = 0^\circ$ cases, there is a considerable improvement when removing the surface hydrogen environment from only the right grain: 35 % in the best of cases (from 5 wt ppm to pure air).

Table 4.4 $F_{máx}$ obtained for the cases with vaiable initial concentration of hydrogen in the right grain $C_{0,grain}$ with $\alpha = 20^\circ$.

$C_{0,right}\ (wt\ ppm)$	$F_{máx}\ (N)$	$u_y\ (10^3\ mm)$
0 (Air)	972.27	3.15
0.5	826.14	2.95
1	760.66	2.80
5	631.47	2.40

Next, the dependence of these inclined probes with the mismatch in the critical energy release rate G_C^b is analyzed. Fixing a left grain value of $G_{C,left}^b = 2.7\ N \cdot mm$, four different probes ranging from $70\,\% G_{C,left}^b$ to $200\,\% G_{C,left}^b$ in their values of $C_{0,right}$ have represented their load-displacement curve in fig. 4.13. Furthermore, a value for the initial hydrogen concentration of $C_0 = C_b = 0.5\ wt\ ppm$ is set for the whole specimen.

At last, the tab. 4.4 represents the peaks of the reaction forces in the fixed surface, as well as their respective displacements. An improvement in the maximum force of 13 % may be obtained in the best of cases (improving $G_{C,right}^b$ from 1.89 $MPa \cdot mm$ to 5.40 $MPa \cdot mm$), considerably similar to the cases with $\alpha = 0^\circ$.

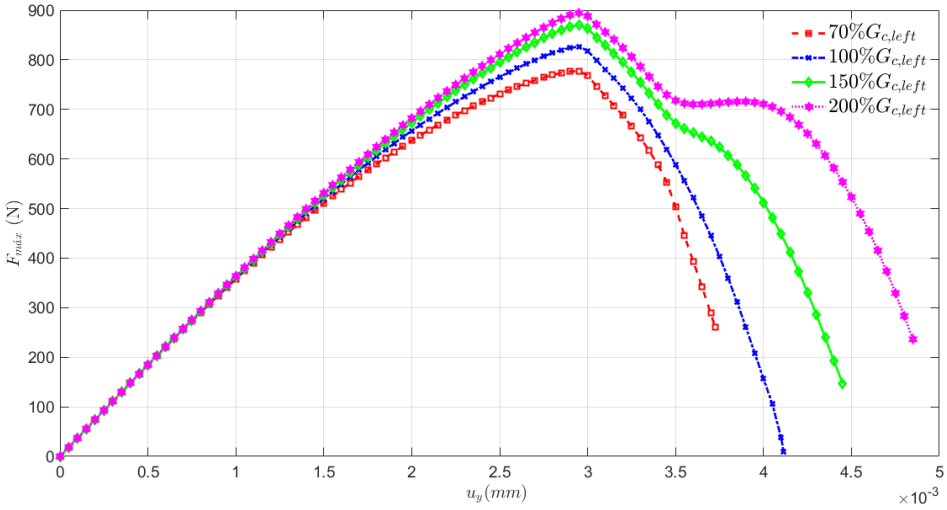

Figure 4.14 Load-displacement curve obtained for the different cases of initial right-grain critical energy release rate $G_{C,right}^b$ with inclined grain boundary of $\alpha = 20^\circ$.

Table 4.5 $F_{máx}$ obtained for the cases with variable critical energy release rate $G_{C,right}^b$ in the right grain with $\alpha = 20^\circ$.

$G_{C,right}^b\ (MPa \cdot mm)$	$F_{máx}\ (N)$	$u_y\ (10^3\ mm)$
1.89 (70 % $G_{C,left}^b$)	776.98	2.95
2.70 (100 % $G_{C,left}^b$)	826.14	2.95
4.05 (150 % $G_{C,left}^b$)	870.13	2.95
5.40 (200 % $G_{C,left}^b$)	894.57	2.95

4.3 Grain boundary modelled with the interface framework

4.3.1 Overview

In order to verify the implementation in the coupling of both bulk & interface frameworks in the same specimen, the same example as the previously studied is used. In fig 4.15, both parts of bulk & interface are clearly distinguished.

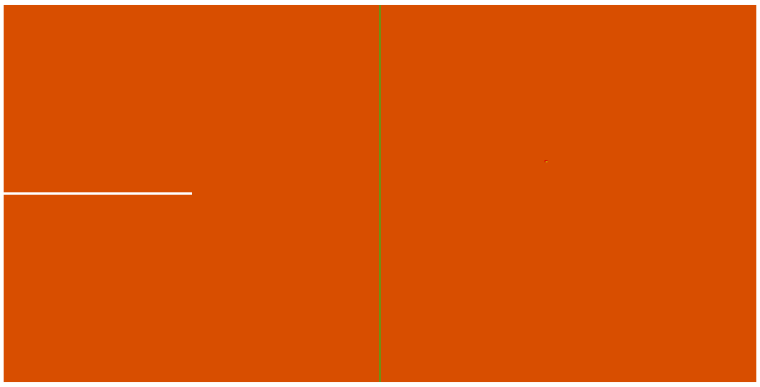

Figure 4.15 Lay-out of the two-grain cracked plate where in different colors is indicated the employment of the bulk or interface code, respectively.

One of the main focus on the preparation of these specimens has been their meshing. Bulk code works with 8 nodes, so reduced scheme integration plane strain elements have been employed (*CPE*8*R*), whereas the interface framework operates with 4 full scheme integration nodes (*CPE*4). Therefore, in order to fulfil the correlation among bulk & interface elements, the latter will be doubled. This is shown in fig. 4.16.

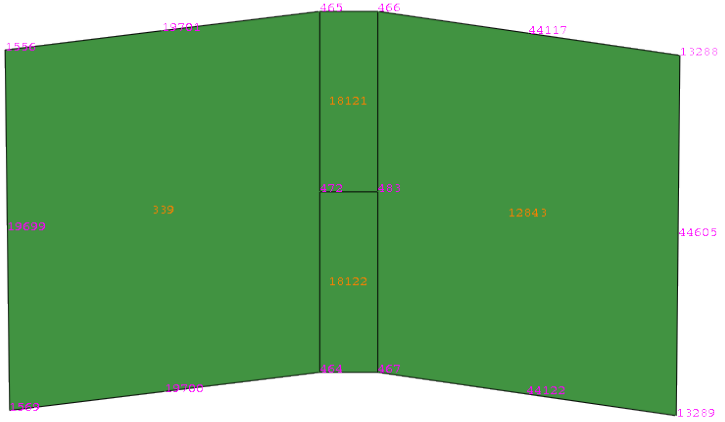

Figure 4.16 Correlation between the *CPE*8*R* bulk and the *CPE*4 interface elements. In the center of each element we see its number, while in the edges and vertices, the node number.

The interface mechanical properties are specified in table 4.6. These values are applied to make the normal and tangential intact interface stiffness $k_{n,0}$ & $k_{t,0}$, equal to the Young modulus of steel E, specified for both grains. In addition to this, if the normal and tangential values are added to eq. 2.33, critical release rates obtained are the same as the ones for both grains.

Table 4.6 Mechanical properties for the interface.

Property	Numerical value
$k_{n,0}$ (MPa/mm)	$2.1 \cdot 10^{5}$
$g_{nc,0}$ (mm)	$0.5 \cdot 10^{-2}$
$g_{nc,1}$ (mm)	$0.1 \cdot 10^{-1}$
$k_{t,0}$ (MPa/mm)	$2.1 \cdot 10^{5}$
$g_{tc,0}$ (mm)	$0.5 \cdot 10^{-2}$
$g_{tc,1}$ (mm)	$0.1 \cdot 10^{-1}$

Besides these aspects, results for this model are similar to those obtained in section 4.2, such as as the representative crack paths in fig. 4.5 (see fig. 4.17). A parametric study for the hydrogen concentration in the interface (see eq. 2.43) has been carried out in the next section.

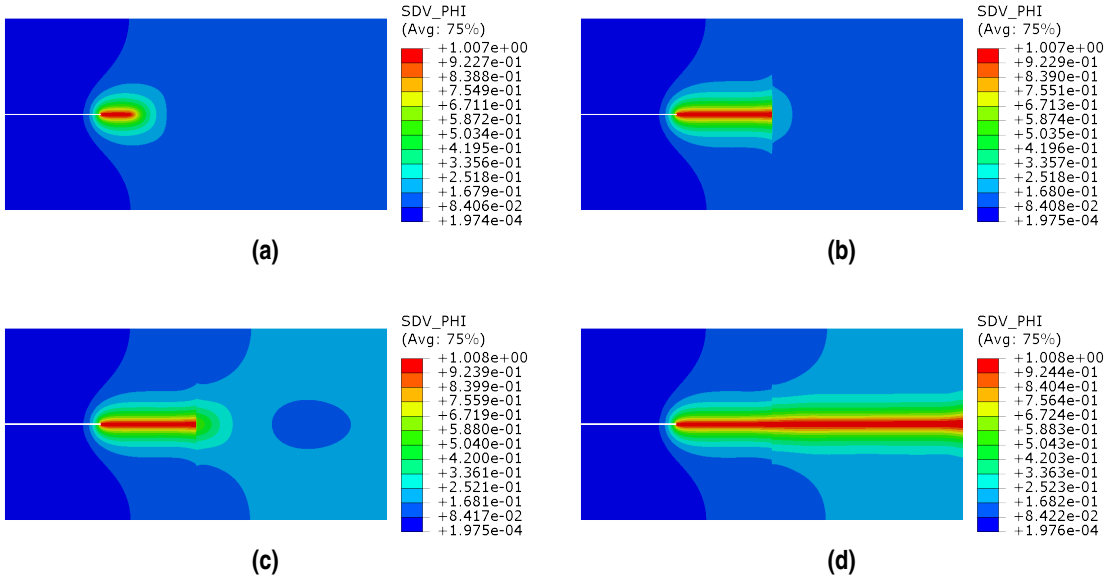

Figure 4.17 Phase field variable map: fracture patterns at different load levels for bulk and interface coupled model.

4.3.2 Cases with different hydrogen concentration in the interface

Four different two grain cases with variable hydrogen concentration in the interface (related to eq. 2.43) have been analyzed until unstable crack propagation. Vertical displacement of these probes can be observed in fig. 4.18.

Furthermore, values for the critical energy release rate of $G_C^b = 2.7\ MPa \cdot mm$ and a initial concentration of hydrogen of $C_0 = C_b = 0.5\ wt\ ppm$ are both fixed for the specimen.

The main result obtained from this further analysis is the load-displacement curve for every case, which is represented in fig. 4.19, along with the previously studied model with ideal grain boundary (which means, without interface model). Comparison among these two types of curves demonstrate two different types of behavior:

- In the ideal grain boundary model, there are only two different zones: initiation and propagation, separated when the slope of the curve changes from positive to negative.
- In the grain boundary modelled with the interface code, in its curve we observe four different zones: crack initiation, first grain collapse, interface delamination and second grain collapse.

In addition to this, it is seen that with the interface model, the maximum vertical displacement is higher than the ideal grain boundary model.

However, if the different interface models are compared, it follows that there is not any difference in their mechanical behaviour among them, according to the load-displacement curve. This may be explained due to the interface energy representing a significantly low value of the total specimen energy. Therefore, it is necessary to model with more grain boundaries in order to observe contrast among these different examples.

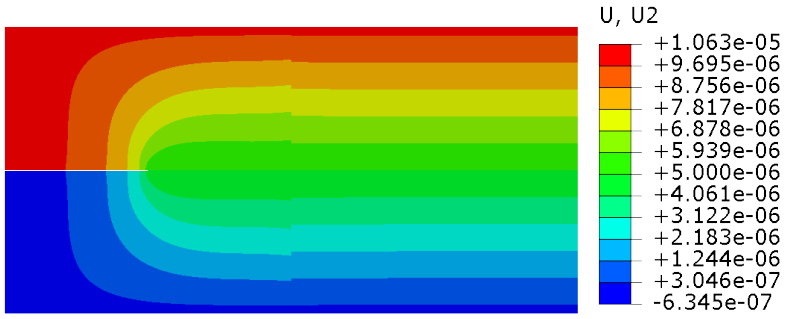

(a)

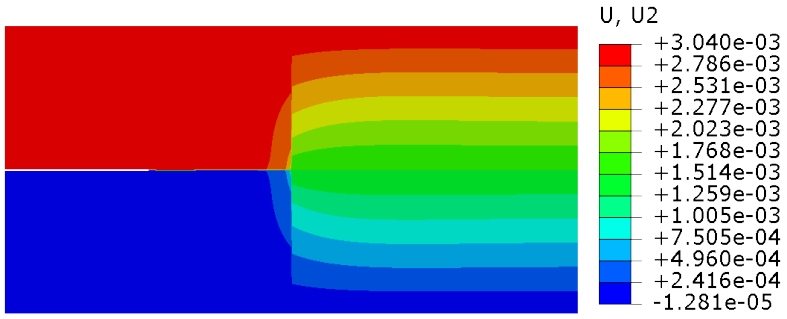

(b)

Figure 4.18 Vertical displacement u_y isocontorn of the probes when: a) the mechanical test starts & b) the crack is propagating through the interface (delamination).

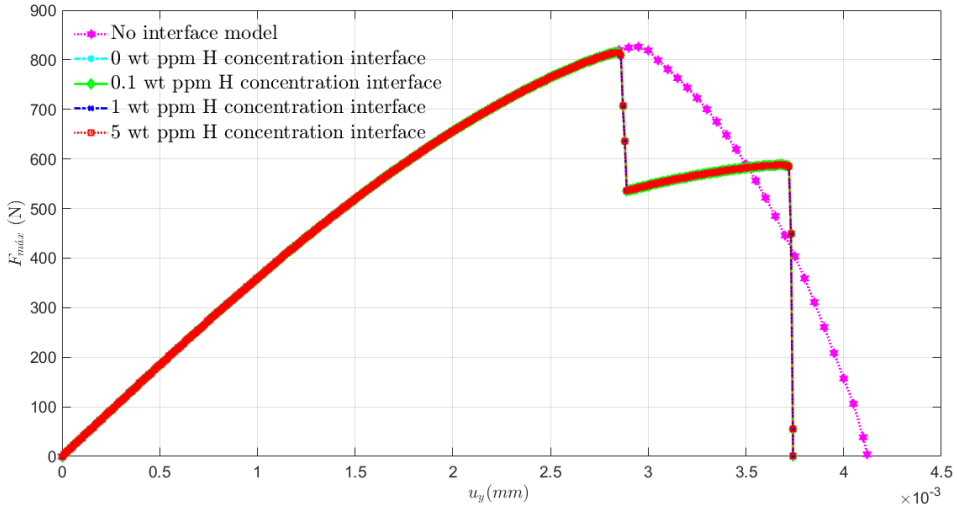

Figure 4.19 Load-displacement curve obtained for the different cases of hydrogen concentration in the interface.

5 Conclusions & Further steps

It has been performed a numerical model to quantify the fracture toughness in coupons submitted to a hydrogen environment which causes them to reduce their energy, depending on its concentration.

This novel framework has been obtained by comibining the bulk code developed by Paneda in [1] & the interface one developed by Paggi and Reinoso in [2]. In this coupled model, originally, only the bulk structure consider the hydrogen influence, so this parameter has been introduced in the interface groundwork by affecting the critical energy release rate.

After implementing, two types of examples have been deeply analyzed in this work using the same probe (a two-grain cracked plate). The first one consisted in verifying the role of hydrogen employing only the bulk framework, studying how the crack propagation is affected by the mismatch in the surfacing hydrogen concentration (a 32 % improvement in the critical force in the best of cases) and in the critical energy release rate (14 %) among both grains. In addition to this, coupons with inclined grain boundaries have also been addressed, where they show one of the limitations of the ideal grain boundary supposition, due to not observing any crack deflection in the numerical models.

The second series of examples consisted in simulating the same probes with the developed novel framework. The difference in the crack trayectory between these examples and the others has been obtained: while in the ideal grain models, initiation and propagation was only observed; in the interface specimens, initiation, first grain collapse, interface delamination & second grain collapse were the observed zones in the load-displacement curve.

However, the potential of the code resides in the possibility of modelling hydrogen coverage in grain boundaries and although, no conclusive results were obtained, this will be the main matter of importance on the next steps of these projects.

First of all, in an immediate future, average hydrogen concentration C will be introduced as a degree of freedom in the interface formulation. Because of this, due to the interface element having 4 elements, 16 DOFs will be employed (4 for horizontal displacements u_x, 4 for vertical displacements u_y, 4 for the phase field parameter ϕ & 4 for the hydrogen concentration C). The average hydrogen concentration will be introduced as the eq. 5.1

$$C = \boldsymbol{N}_C \boldsymbol{M}_C \bar{C} = \boldsymbol{B}_C \bar{C} \tag{5.1}$$

where M_C is the average operator and $\boldsymbol{B}_C$, the compatibility operator for the hydrogen concentration C. This is similar to eq. 5.1. However, some clarifications must be done about this parameter: it is introduced as a material property in the code and it is averaged between the number of nodes. Due to it remaining constant throughout the whole process, the atributed residual for hydrogen concentration $r^C_{int} = 0$.

The constitutive matrix for the hydrogen variable is therefore, equated to the identity, in order to the concentration to remain constant, $\boldsymbol{K}^{CC} = \boldsymbol{I}$. Then, the coupled system of equations for displacement, phase field & hydrogen concentration parameters will be

$$\begin{bmatrix} \boldsymbol{K}^{\boldsymbol{uu}} & \boldsymbol{K}^{\boldsymbol{u}\phi} & \boldsymbol{0} \\ \boldsymbol{K}^{\phi\boldsymbol{u}} & \boldsymbol{K}^{\phi\phi} & \boldsymbol{0} \\ \boldsymbol{0} & \boldsymbol{0} & \boldsymbol{I} \end{bmatrix} \begin{bmatrix} \delta \boldsymbol{u} \\ \delta \phi \\ \delta C \end{bmatrix} = \begin{bmatrix} \boldsymbol{r}^{\boldsymbol{u}}_{int} \\ r^{\phi}_{int} \\ 0 \end{bmatrix} \tag{5.2}$$

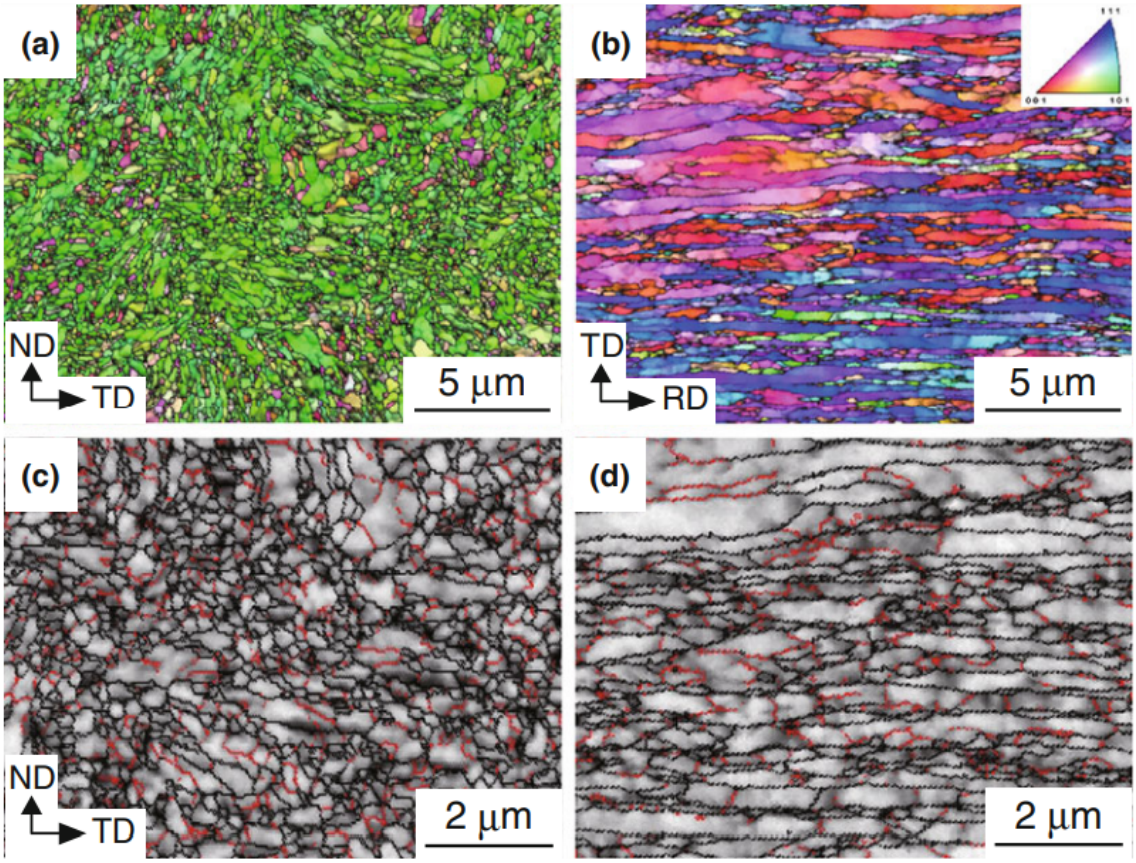

Figure 5.1 Maps (a), (b) & image quality maps (c), (d) employed to show the grain structure in the longitudinal and transversal direction, respectively in a tempformed steel [70].

Currently, the project has implemented the equations system of 5.2 for the specimen, however, no conclusive results have been obtained from this experiment due to convergence problems, because residuals obtained in the interface are too high compared to the step increments. In order to solve this problem, some low step probes are thought to be started soon, or residual tolerance will be changed: the amount of this parameters to be changed will depend on looking for an equilibrium between running time and accuracy of the results.

Another target which will be attempted shortly after is the modelization of bulk & interface specimens with an inclined grain boundary. What is sought by these experiments is to see how crack deflection works when it is propagating through the interface. Such experiments require to provide the interface with more robustness to fulfil them.

What follows up next is one of the main objectives which are seeked for this project: the exportation of this model to multi-grain specimens. For instance, in fig. 5.1 we have images of different grain structures in a tempformed steel. Both images correspond to different planes (the first one parallel to the rolling direction, while the other is perpendicular to it). The developed framework is thought to simulate thermo-mechanical tests employing such structures.

Achieving to implement the framework in such structure (defining every grain with the bulk code & their respective boundaries with the interface one) would open the door to different interesting applications for this project: one possible stream for it could be the theoretical evaluation of the grain boundary contamination with hydrogen. As it may have been observed in the development of the bulk code by Martínez-Pañeda [1] or in the previous work by other authors such as [71], the phase field model with hydrogen segregation in the bulk has been considerably addressed by other authors. Nevertheless, the phase field-CZM framework for fracture has not been theoretically implemented. The next step for this instance will be the searching of examples which have studied this model with hydrogen, like [72]. After analyzing the background, it will be applied to the framework an interface energy degradation by the hydrogen coverage via a phenomenologic manner.

Another example which may show the potential the novel framework holds resides on the study of the competition between intergranular and transgranular fracture. The main fact of this possible study is related

to the further analysis of different materials which show these inestabilities. For example, nickel superalloys, as it is seen in fig. 5.2, show both types of fracture because of void coalescence (intergranular) or cleavage (transgranular).

The last proposed example is about the implementation of plasticity in the framework. Every suggested hydrogen embrittlement model proposed until now only predicts brittle fracture; therefore, none of them has been able to model ductile transgranular fracture. A possibility for this experiment consists in modelling ductile fracture in the bulk framework, while in the interface, brittle fracture is employed. In order to do this, plasticity must be added to the bulk framework and assign a critical energy release rate G_c higher in the order of $100 - 1000kJ$, in addition to a length scale ℓ also superior. With the addition of hydrogen in the grain boundaries, fracture should turn from transgranular to intergranular, due to metals suffering brittle fracture in presence of hydrogen.

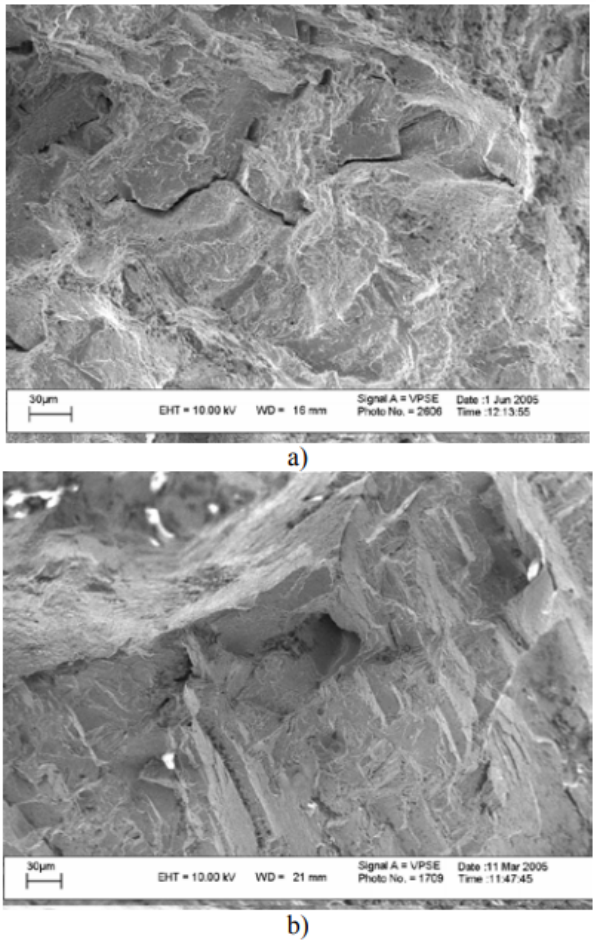

Figure 5.2 Micrographs showing a nickel superalloy GTD-11 specimen with a) fractured grain boundaries and b) transgranular fracture [73].

List of Figures

List of Tables

Bibliografía

[1] E. Martínez-Pañeda, A. Golahmar, and C. F. Niordson, "A phase field formulation for hydrogen assisted cracking," *Computer Methods in Applied Mechanics and Engineering*, vol. 342, pp. 742 – 761, 2018.

[2] M. Paggi and J. Reinoso, "Revisiting the problem of a crack impinging on an interface:a modeling framework for the interaction between the phase field approach for brittle fracture and the interface cohesive zone model," *Computer Methods in Applied Mechanics and Engineering*, vol. 321, pp. 145 – 172, 2017.

[3] J. W. H. and T. William, "Ii. on some remarkable changes produced in iron and steel by the action of hydrogen and acids," *Royal Society*, vol. 23, 1875. Issue 156-163.

[4] Y. S. Kim, S. S. Kim, and B. H. Choe, "The role of hydrogen in hydrogen embrittlement of metals: The case of stainless steel," *Metals*, vol. 9, no. 4, 2019.

[5] A. Atrens, Q. Liu, C. Tapia, E. Gray, B. Irwanto, J. Venezuela, and Q. Liu, "Influence of hydrogen on steel components for clean energy," *Corrosion and Materials Degradation*, vol. 1, p. 2, 06 2018.

[6] L. Industrial Metallurgists, "Hydrogen embrittlement of steel."

[7] M. Faller and P. Richner, "Material selection of safety-relevant components in indoor swimming pools," *Materials and Corrosion*, vol. 54, no. 5, pp. 331–338.

[8] Y. Fan, B. Zhang, J. Wang, E.-H. Han, and W. Ke, "Effect of grain refinement on the hydrogen embrittlement of 304 austenitic stainless steel," *Journal of Materials Science & Technology*, 2019.

[9] S. Shen, X. Song, Q. Li, X. Li, R. Zhu, and G. Yang, ""a study on stress corrosion cracking and hydrogen embrittlement of jethete m152 martensitic stainless steel"," *Materials Science and Engineering: A*, vol. 740-741, pp. 243 – 251, 2019.

[10] S. Wang, D. Xu, B. Wang, L. Sheng, E. Han, and C. Dong, "Effect of solution treatment on stress corrosion cracking behavior of an as-forged mg-zn-y-zr alloy," *Scientific reports*, vol. 6, p. 29471, 07 2016.

[11] M. B. Kannan and W. Dietzel, "Pitting-induced hydrogen embrittlement of magnesium–aluminium alloy," *Materials & Design*, vol. 42, pp. 321 – 326, 2012.

[12] Z. Zhang, K. L. Moore, G. McMahon, R. Morana, and M. Preuss, "On the role of precipitates in hydrogen trapping and hydrogen embrittlement of a nickel-based superalloy," *Corrosion Science*, vol. 146, pp. 58 – 69, 2019.

[13] F. Han, S. He, M. Liu, and X. Zhou, "Hydrogen embrittlement susceptibility of a ni-16mo-7cr base superalloy," *Materials Science and Engineering: A*, vol. 733, pp. 291 – 298, 2018.

[14] X. Li, J. Zhang, E. Akiyama, Q. Fu, and Q. Li, "Hydrogen embrittlement behavior of inconel 718 alloy at room temperature," *Journal of Materials Science & Technology*, vol. 35, no. 4, pp. 499 – 502, 2019.

[15] L. Vergani, C. Colombo, G. Gobbi, F. M. Bolzoni, and G. Fumagalli, "Hydrogen effect on fatigue behavior of a quenched&tempered steel," *Procedia Engineering*, vol. 74, pp. 468 – 471, 2014. XVII International Colloquium on Mechanical Fatigue of Metals (ICMFM17).

[16] E. Martínez-Pañeda, C. F. Niordson, and R. P. Gangloff, "Strain gradient plasticity-based modeling of hydrogen environment assisted cracking," *Acta Materialia*, vol. 117, pp. 321 – 332, 2016.

[17] P. Novak, R. Yuan, B. Somerday, P. Sofronis, and R. Ritchie, "A statistical, physical-based, micro-mechanical model of hydrogen-induced intergranular fracture in steel," *Journal of the Mechanics and Physics of Solids*, vol. 58, no. 2, pp. 206 – 226, 2010.

[18] C. Ayas, V. Deshpande, and N. Fleck, "A fracture criterion for the notch strength of high strength steels in the presence of hydrogen," *Journal of the Mechanics and Physics of Solids*, vol. 63, pp. 80 – 93, 2014.

[19] S. del Busto, C. Betegón, and E. Martínez-Pañeda, "A cohesive zone framework for environmentally assisted fatigue," *Engineering Fracture Mechanics*, vol. 185, pp. 210 – 226, 2017. XVIII International Colloquium Mechanical Fatigue of Metals.

[20] S. Serebrinsky, E. Carter, and M. Ortiz, "A quantum-mechanically informed continuum model of hydrogen embrittlement," *Journal of the Mechanics and Physics of Solids*, vol. 52, no. 10, pp. 2403 – 2430, 2004.

[21] N. Valoroso and R. Fedele, "Characterization of a cohesive-zone model describing damage and de-cohesion at bonded interfaces. sensitivity analysis and mode-i parameter identification," *International Journal of Solids and Structures*, vol. 47, no. 13, pp. 1666 – 1677, 2010.

[22] K. J. Koester, J. W. Ager III, and R. O. Ritchie, "The true toughness of human cortical bone measured with realistically short cracks," *Nature Materials*, vol. 7, p. 672, Jun 2008. Article.

[23] F. Barthelat, H. Tang, P. Zavattieri, C.-M. Li, and H. Espinosa, "On the mechanics of mother-of-pearl: A key feature in the material hierarchical structure," *Journal of the Mechanics and Physics of Solids*, vol. 55, no. 2, pp. 306 – 337, 2007.

[24] P. Fratzl, O. Kolednik, F. D. Fischer, and M. N. Dean, "The mechanics of tessellations – bioinspired strategies for fracture resistance," *Chem. Soc. Rev.*, vol. 45, pp. 252–267, 2016.

[25] B. L. Smith, T. E. Schäffer, M. Viani, J. B. Thompson, N. A. Frederick, J. Kindt, A. Belcher, G. D. Stucky, D. E. Morse, and P. K. Hansma, "Molecular mechanistic origin of the toughness of natural adhesives, fibres and composites," *Nature*, vol. 399, no. 6738, pp. 761–763, 1999.

[26] F. Barthelat, "Architectured materials in engineering and biology: fabrication, structure, mechanics and performance," *International Materials Reviews*, vol. 60, no. 8, pp. 413–430, 2015.

[27] J. W. Dunlop, R. Weinkamer, and P. Fratzl, "Artful interfaces within biological materials," *Materials Today*, vol. 14, no. 3, pp. 70 – 78, 2011.

[28] G. Francfort and J.-J. Marigo, "Revisiting brittle fracture as an energy minimization problem," *Journal of the Mechanics and Physics of Solids*, vol. 46, no. 8, pp. 1319 – 1342, 1998.

[29] B. Bourdin, G. Francfort, and J.-J. Marigo, "Numerical experiments in revisited brittle fracture," *Journal of the Mechanics and Physics of Solids*, vol. 48, no. 4, pp. 797 – 826, 2000.

[30] B. Bourdin, G. A. Francfort, and J.-J. Marigo, "The variational approach to fracture," *Journal of Elasticity*, vol. 91, pp. 5–148, Apr 2008.

[31] C. Miehe, F. Welschinger, and M. Hofacker, "Thermodynamically consistent phase-field models of fracture: Variational principles and multi-field fe implementations," *International Journal for Numerical Methods in Engineering*, vol. 83, no. 10, pp. 1273–1311.

[32] M. J. Borden, T. J. Hughes, C. M. Landis, and C. V. Verhoosel, "A higher-order phase-field model for brittle fracture: Formulation and analysis within the isogeometric analysis framework," *Computer Methods in Applied Mechanics and Engineering*, vol. 273, pp. 100 – 118, 2014.

[33] M. J. Borden, T. J. Hughes, C. M. Landis, A. Anvari, and I. J. Lee, "A phase-field formulation for fracture in ductile materials: Finite deformation balance law derivation, plastic degradation, and stress triaxiality effects," *Computer Methods in Applied Mechanics and Engineering*, vol. 312, pp. 130 – 166, 2016. Phase Field Approaches to Fracture.

[34] C. Miehe, L.-M. Schänzel, and H. Ulmer, "Phase field modeling of fracture in multi-physics problems. part i. balance of crack surface and failure criteria for brittle crack propagation in thermo-elastic solids," *Computer Methods in Applied Mechanics and Engineering*, vol. 294, pp. 449 – 485, 2015.

[35] C. Miehe, M. Hofacker, L.-M. Schänzel, and F. Aldakheel, "Phase field modeling of fracture in multi-physics problems. part ii. coupled brittle-to-ductile failure criteria and crack propagation in thermo-elastic–plastic solids," *Computer Methods in Applied Mechanics and Engineering*, vol. 294, pp. 486 – 522, 2015.

[36] J. Reinoso, M. Paggi, and C. Linder, "Phase field modeling of brittle fracture for enhanced assumed strain shells at large deformations: formulation and finite element implementation," *Computational Mechanics*, vol. 59, pp. 981–1001, Jun 2017.

[37] V. Carollo, J. Reinoso, and M. Paggi, "A 3d finite strain model for intralayer and interlayer crack simulation coupling the phase field approach and cohesive zone model," *Composite Structures*, vol. 182, pp. 636 – 651, 2017.

[38] J. R. e. a. A. Quintanas-Corominas, A. Turon, "A phase field approach enhanced with a cohesive zone model for modeling delamination induced by matrix cracking, computer methods in applied mechanics and engineering," *Computer Methods in Applied Mechanics and Engineering*, 2019.

[39] OCZ, Rlt, and Jzz, "Preface for volume i," in *The Finite Element Method Set (Sixth Edition)* (O. Zienkiewicz, R. Taylor, and J. Zhu, eds.), pp. xiii – xiv, Oxford: Butterworth-Heinemann, sixth edition ed., 2005.

[40] W. Lee, Y.-H. Yoo, and H. Shin, "Reconsideration of crack deflection at planar interfaces in layered systems," *Composites Science and Technology*, vol. 64, no. 15, pp. 2415 – 2423, 2004. Developments in carbon nanotube and nanofibre reinforced polymers.

[41] N. D. Parab and W. W. Chen, "Crack propagation through interfaces in a borosilicate glass and a glass ceramic," *International Journal of Applied Glass Science*, vol. 5, no. 4, pp. 353–362.

[42] C. Miehe, M. Hofacker, and F. Welschinger, "A phase field model for rate-independent crack propagation: Robust algorithmic implementation based on operator splits," *Computer Methods in Applied Mechanics and Engineering*, vol. 199, no. 45, pp. 2765 – 2778, 2010.

[43] M. J. Borden, C. V. Verhoosel, M. A. Scott, T. J. Hughes, and C. M. Landis, "A phase-field description of dynamic brittle fracture," *Computer Methods in Applied Mechanics and Engineering*, vol. 217-220, pp. 77 – 95, 2012.

[44] H. Amor, J.-J. Marigo, and C. Maurini, "Regularized formulation of the variational brittle fracture with unilateral contact: Numerical experiments," *Journal of the Mechanics and Physics of Solids*, vol. 57, no. 8, pp. 1209 – 1229, 2009.

[45] C. V. Verhoosel and R. de Borst, "A phase-field model for cohesive fracture," *International Journal for Numerical Methods in Engineering*, vol. 96, no. 1, pp. 43–62.

[46] B. Bourdin, G. A. Francfort, and J.-J. Marigo, "The variational approach to fracture," *Journal of Elasticity*, vol. 91, pp. 5–148, Apr 2008.

[47] V. Lubarda, D. Krajcinovic, and S. Mastilovic, "Damage model for brittle elastic solids with unequal tensile and compressive strengths," *Engineering Fracture Mechanics*, vol. 49, no. 5, pp. 681 – 697, 1994.

[48] B. D. Coleman and W. Noll, "The thermodynamics of elastic materials with heat conduction and viscosity," *Archive for Rational Mechanics and Analysis*, vol. 13, pp. 167–178, Dec 1963.

[49] M. A. Msekh, J. M. Sargado, M. Jamshidian, P. M. Areias, and T. Rabczuk, "Abaqus implementation of phase-field model for brittle fracture," *Computational Materials Science*, vol. 96, pp. 472 – 484, 2015. Special Issue Polymeric Composites.

[50] J. Williams and H. Hadavinia, "Analytical solutions for cohesive zone models," *Journal of the Mechanics and Physics of Solids*, vol. 50, no. 4, pp. 809 – 825, 2002.

[51] V. Mantič, L. Távara, A. Blázquez, E. Graciani, and F. París, "A linear elastic-brittle interface model: application for the onset and propagation of a fibre-matrix interface crack under biaxial transverse loads," *International Journal of Fracture*, vol. 195, pp. 15–38, Sep 2015.

[52] J. Reinoso, A. Blázquez, L. Távara, F. París, and C. Arellano, "Damage tolerance of composite runout panels under tensile loading," *Composites Part B: Engineering*, vol. 96, pp. 79 – 93, 2016.

[53] M. Paggi and J. Reinoso, "An anisotropic large displacement cohesive zone model for fibrillar and crazing interfaces," *International Journal of Solids and Structures*, vol. 69-70, pp. 106 – 120, 2015.

[54] D. Jiang and E. A. Carter, "First principles assessment of ideal fracture energies of materials with mobile impurities: implications for hydrogen embrittlement of metals," *Acta Materialia*, vol. 52, no. 16, pp. 4801 – 4807, 2004.

[55] A. Alvaro, I. T. Jensen, N. Kheradmand, O. Løvvik, and V. Olden, "Hydrogen embrittlement in nickel, visited by first principles modeling, cohesive zone simulation and nanomechanical testing," *International Journal of Hydrogen Energy*, vol. 40, no. 47, pp. 16892 – 16900, 2015. Special issue on 1st International Conference on Hydrogen Storage, Embrittlement and Applications (Hy-SEA 2014), 26-30 October 2014, Rio de Janeiro, Brazil.

[56] E. Tanné, T. Li, B. Bourdin, J.-J. Marigo, and C. Maurini, "Crack nucleation in variational phase-field models of brittle fracture," *Journal of the Mechanics and Physics of Solids*, 09 2017.

[57] N. Moës and T. Belytschko, "Extended finite element method for cohesive crack growth," *Engineering Fracture Mechanics*, vol. 69, no. 7, pp. 813 – 833, 2002.

[58] J. Rice, "Mathematical analysis in the mechanics of fracture," *An Advanced Treatise, H. Liebowitz Ed., Vol.*, vol. 2, 01 1979.

[59] M. E. Gurtin, E. Fried, and L. Anand, *The Mechanics and Thermodynamics of Continua*. Cambridge University Press, 2010.

[60] C. V. D. Leo and L. Anand, "Hydrogen in metals: A coupled theory for species diffusion and large elastic–plastic deformations," *International Journal of Plasticity*, vol. 43, pp. 42 – 69, 2013.

[61] E. Martínez-Pañeda and C. Betegón, "Modeling damage and fracture within strain-gradient plasticity," *International Journal of Solids and Structures*, vol. 59, pp. 208 – 215, 2015.

[62] E. Martínez-Pañeda and C. Niordson, "On fracture in finite strain gradient plasticity," *International Journal of Plasticity*, vol. 80, pp. 154 – 167, 2016.

[63] E. Martínez-Pañeda, S. Natarajan, and S. Bordas, "Gradient plasticity crack tip characterization by means of the extended finite element method," *Computational Mechanics*, vol. 59, pp. 831–842, May 2017.

[64] J. P. Hirth, "Effects of hydrogen on the properties of iron and steel," *Metallurgical Transactions A*, vol. 11, pp. 861–890, Jun 1980.

[65] Y. Zhao, B.-X. Xu, P. Stein, and D. Gross, "Phase-field study of electrochemical reactions at exterior and interior interfaces in li-ion battery electrode particles," *Computer Methods in Applied Mechanics and Engineering*, vol. 312, pp. 428 – 446, 2016. Phase Field Approaches to Fracture.

[66] A. Cheng and N.-Z. Chen, "Fatigue crack growth modelling for pipeline carbon steels under gaseous hydrogen conditions," *International Journal of Fatigue*, vol. 96, pp. 152 – 161, 2017.

[67] M. Paggi and P. Wriggers, "Stiffness and strength of hierarchical polycrystalline materials with imperfect interfaces," *Journal of the Mechanics and Physics of Solids*, vol. 60, p. 557–572, 04 2012.

[68] M. Paggi and J. Reinoso, "An anisotropic large displacement cohesive zone model for fibrillar and crazing interfaces," *International Journal of Solids and Structures*, vol. 107, 06 2015.

[69] J. Reinoso and M. Paggi, "A consistent interface element formulation for geometrical and material nonlinearities," *Computational Mechanics*, vol. 54, 12 2014.

[70] Y. Nie, Y. Kimura, T. Inoue, F. Yin, E. Akiyama, and K. Tsuzaki, "Hydrogen embrittlement of a 1500-mpa tensile strength level steel with an ultrafine elongated grain structure," *Metallurgical and Materials Transactions A*, vol. 43, pp. 1670–1687, May 2012.

[71] C. Hueter, P. Shanthraj, E. Mceniry, R. Spatschek, T. Hickel, A. Tehranchi, X. Guo, and F. Roters, "Multiscale modelling of hydrogen transport and segregation in polycrystalline steels," *Metals*, vol. 8, p. 430, 06 2018.

[72] J.-Y. Wu, T. Mandal, and V. P. Nguyen, "A phase-field regularized cohesive zone model for hydrogen assisted cracking," *Computer Methods in Applied Mechanics and Engineering*, 08 2019.

[73] S. Sajjadi and S. Zebarjad, "Study of fracture mechanisms of a ni-base superalloy at different temperatures," *Journal of Achievements in Materials and Manufacturing Engineering*, vol. 18, 08 2006.